A RECORD OF LOW-TEMPERATURE ASTEROIDAL PROCESSES OF AMOEBOID OLIVINE AGGREGATES FROM THE KAINSAZ CO3.2 CHONDRITE

Jangmi Han [a,b,c,*], Changkun Park [d], and Adrian J. Brearley [a]

[a] Department of Earth and Planetary Sciences, University of New Mexico, Albuquerque, New Mexico 87131, USA

[b] Lunar and Planetary Institute, USRA, 3600 Bay Area Boulevard, Houston, TX 77058, USA

[c] Astromaterials Research and Exploration Science, NASA Johnson Space Center, 2101 NASA Parkway, Houston, TX 77058, USA

[d] Division of Earth Sciences, Korea Polar Research Institute, 26 Songdomirae-ro, Yeonsu-gu, Incheon 21990, South Korea

*Corresponding author. Email address: jhan28@central.uh.edu (J. Han). Present address: Department of Earth and Atmospheric Sciences, University of Houston, Houston, TX 77204, USA.

Submitted to *Geochimica et Cosmochimica Acta*, August 24, 2021

Revised, February 3, 2022

ABSTRACT

Amoeboid olivine aggregates (AOAs) from the Kainsaz CO3.2 chondrite were analyzed using transmission electron microscopy in order to gain a more complete understanding of thermal metamorphism on the parent body and the role of fluids during metamorphic heating. The Kainsaz AOAs are dominated by strongly zoned, fine-grained, olivine grains ($Fa_{2\text{-}31}$) with heterogeneous Fe enrichments along the grain boundaries, which are interpreted as the result of Fe^{2+}-Mg^{2+} interdiffusion with the matrix during thermal metamorphism. However, our diffusion calculations show that such AOA olivine zoning and compositions cannot be produced by a simple diffusional exchange during metamorphic heating, unlike chondrule olivine zoning and compositions. In addition, fine-grained ferroan olivine overgrowths occur heterogeneously in crystallographic continuity with olivines on the AOA exteriors. The overgrowths ($Fa_{33\text{-}36}$) are

compositionally distinct from the underlying AOA olivines and are not fully equilibrated with the matrix olivines ($Fa_{\sim 20\text{-}55}$). The ferroan olivine overgrowths likely formed by precipitation from fluids in an epitaxial relationship with forsteritic olivine on the edges of AOAs. Texturally and compositionally diverse chromite grains are also observed along olivine grain boundaries, in olivine grains, and in pore spaces between olivine grains. They share a similar crystallographic orientation relationships with adjacent olivine, suggestive of their formation by exsolution and/or epitaxial growth. Collectively, these observations provide evidence for the mobilization of Fe, Mg, Si, Cr, and Al in the presence of fluids along olivine grain boundaries and into olivine grains during thermal metamorphism. We conclude that in Kainsaz AOAs, the strong zonation development in individual olivine grains and the formation of ferroan olivine overgrowths and chromite grains were a fluid-driven process that occurred at relatively low temperatures (<500°C), during the cooling history of the CO3 chondrite parent body, following the peak of thermal metamorphism.

Keywords: Amoeboid olivine aggregates, transmission electron microscopy, thermal metamorphism, fluid, CO3 chondrites.

1. INTRODUCTION

The CO3 chondrites are the only carbonaceous chondrite group that has been proven to show a well-defined sequence of increasing degree of thermal metamorphism based on a diverse range of petrologic and mineralogical characteristics (e.g., McSween, 1977; Scott and Jones, 1990; Sears et al., 1991; Chizmadia et al., 2002; Grossman and Brearley, 2005; Bonal et al., 2007; Kimura et al., 2008; Imae and Nakamuta, 2018). Based on the compositions of olivine and pyroxene in chondrules and the degree of textural recrystallization from six CO3 chondrites, McSween (1977) first stated that CO3 chondrites comprise a metamorphic series: stage I, II, and III. Later, Scott and Jones (1990) refined the metamorphic subtypes 3.0 to 3.7 using the distribution of FeO contents in olivine and pyroxene and minor element compositions in Fe,Ni metal. Chizmadia et al. (2002) focused on amoeboid olivine aggregates (AOAs) to quantify the effects of thermal metamorphism on CO3 chondrites in view of the fact that AOAs are sensitive indicators of alteration due to their fine-grained nature. Based on the systematic change in thickness of ferroan olivine veins and olivine compositional distributions, Chizmadia et al. (2002) refined the metamorphic subtypes 3.0 to 3.8 and suggested that the subtypes of all other

CO3 chondrites assigned by Scott and Jones (1990) should be increased by 0.1, except for CO3.0 chondrites such as Allan Hills (ALH) A77307, Colony, and Yamato (Y) 81020. There are some differences in the petrologic subtype of individual CO chondrites depending on the classification scheme used, but overall there is generally good consistency between the petrologic sequences based on different classification techniques.

The Kainsaz CO chondrite was originally classified as Type I in McSween (1977) and later assigned as petrologic subtype 3.1 by Scott and Jones (1990). However, more recently this meteorite has been classified as subtype 3.2 in the literature, as recommended in the Meteoritical Bulletin Database. This assignment was also suggested by Grossman and Brearley (2005), based on a comparison with systematic variations in Cr content of ferroan olivine in type II chondrules from ordinary chondrites, consistent with Chizmadia et al. (2002) and most other studies of silicate and metal compositions (e.g., Sears et al., 1991; Tomeoka and Itoh, 2004). In the following, we assign Kainsaz as petrologic subtype 3.2.

The progressive changes in mineralogy, chemistry, and isotopic composition with increasing petrologic subtype from 3.0 to 3.8 in CO3 chondrites have been attributed to complex, combined processes of fluid-driven metasomatism and thermal metamorphism on asteroidal bodies (Brearley and Krot, 2013 for a recent review). These effects include, for example, the formation of secondary alteration products such as nepheline, replacing primary melilite and anorthite in Ca-Al-rich inclusions (CAIs) in Kainsaz and Ornans (CO3.4). This alteration is correlated with the development of bimodal oxygen isotopic compositions of spinel and diopside enriched in ^{16}O and melilite and secondary minerals depleted in ^{16}O, compared with the uniformly ^{16}O-rich phases such as hibonite, melilite, spinel, diopside, and anorthite in CAIs in the CO3.0 chondrites Colony and Y81020 (Wasson et al., 2001; Itoh et al., 2004). A progressive heavy oxygen-isotope enrichment along with the addition of FeO in melilite are also positively correlated with petrologic subtype in CO3 chondrites (Wasson et al., 2001; Itoh et al., 2004). These studies suggest that CO3 chondrites were subjected to metasomatism generating Fe- and Na-rich minerals in CAIs during thermal metamorphism and that oxygen isotopic exchange with a fluid on the parent body changed the composition of minerals in CAIs from ^{16}O-rich to ^{16}O-poor.

In CO3 chondrites, AOAs are very fine-grained (Chizmadia et al., 2002; Han and Brearley, 2015, 2016) and thus are sensitive recorders of the effects of parent body

metasomatism and metamorphism, particularly at the very earliest stages. In this study, we present textural, mineralogical, and chemical observations of AOAs from Kainsaz using transmission electron microscopy (TEM) and compare them with the primary nebular record of AOAs in ALHA77307 presented in Han and Brearley (2015, 2016). Chizmadia et al. (2002) described the incipient formation of ferroan olivine along grain boundaries in AOAs from the CO3.2 chondrites Kainsaz, Rainbow, and Y82050 as a response to fluid-assisted thermal metamorphism. Based on these observations, we focused on AOAs in Kainsaz, which is a fall and hence has not been affected by terrestrial alteration, unlike Rainbow and Y82050. The goal of this study is to provide a comprehensive understanding of how secondary parent body alteration modified the primary mineralogy and textures of AOAs that formed in the early solar nebula and hence obtain insights into the processes and conditions of parent body alteration that affected Kainsaz AOAs. We examine the formation history of ferroan olivine and associated phases in the AOAs that has important implications for the role of fluids during parent body alteration.

2. ANALYTICAL METHODS

We located 101 AOAs from an area of ~30 mm^2 of a thin section of Kainsaz (i.e., 3.4 inclusion/mm^2), using a mosaic of backscattered electron (BSE) images and full elemental X-ray maps of the thin section obtained using a FEI Quanta 3D field emission gun scanning electron microscope (SEM)/focused ion beam (FIB) instrument fitted with an EDAX Apollo 40 SDD energy dispersive spectroscopy (EDS) system with Genesis software at the University of New Mexico (UNM). Individual AOAs were characterized in detail using the same instrument. Quantitative wavelength-dispersive spectrometer analyses of olivine in Kainsaz AOAs were obtained using a JEOL JXA-8200 electron probe micro-analyzer (EPMA) at UNM. All analyses were obtained using a 15 kV accelerating voltage, 20 nA beam current, and a focused 1-μm beam. Elemental calibration was carried out using CM Taylor Company Microprobe Standards as follows: Na on albite, Mg and Si on olivine, K on orthoclase, Ca on diopside, Ti on rutile, V on V metal, Cr on chromite, Mn on spessartine, Al on orthoclase or corundum, and Fe on olivine or almandine. Data were reduced using the modified ZAF correction procedure. EA1 includes the full EPMA data set of AOA olivine compositions from Kainsaz, as well as ALHA77307 reported in Han and Brearley (2015), used for this study.

In this study, four AOAs (08, 16, 34, and 75; Figs. 1-2), which contain well-developed FeO-rich veins along olivine grain boundaries, were selected for a detailed TEM study. A total of five FIB section were prepared across several olivine grains on the AOA edges, using the FEI Quanta 3D field emission gun SEM/FIB instruments at UNM and NASA Johnson Space Center (JSC). Initially, each FIB section from three AOAs 08, 34, and 75 were studied using a JEOL 2010 high resolution TEM and a JEOL 2010F field emission gun scanning TEM at UNM. Later, two FIB sections from one AOA 16 were examined using a JEOL 2500 SE field emission scanning TEM at NASA JSC. All TEMs were operated at 200 kV. Characterization of the microstructures and mineralogy of the FIB sections was carried out using various TEM techniques such as bright-field TEM (BF-TEM), high-resolution TEM (HRTEM), bright-field and dark-field scanning TEM (BF- and DF-STEM), and electron diffraction. Digital TEM images were acquired and processed using GATAN Digital Microscopy Suite imaging software. In addition, quantitative microanalyses were obtained using an Oxford INCA 200 energy dispersive X-ray (EDX) spectroscopy system with Oxford Pentafet ultrathin window detector at UNM and a Thermo-Noran thin window EDX spectrometer at NASA JSC. Data were reduced using the Cliff-Lorimer thin film approximation using experimental and theoretical k-factors, and are present in EA1.

3. RESULTS

3.1. Petrology and mineralogy of Kainsaz AOAs

In Kainsaz, AOAs are typically irregularly-shaped and porous objects that range in size from 25 μm to 650 μm. The AOAs in Kainsaz are dominated by olivine ($Fa_{\sim 1\text{-}22}$) with minor Ca,Al-rich phases and Fe,Ni metal. The textural relationships between olivine and other constituent phases in Kainsaz AOAs are generally similar to those in ALHA77307 described in Han and Brearley (2015, 2016) and are consistent with the observations of Chizmadia et al. (2002). Here we describe the characteristics of olivine in Kainsaz AOAs that differ from those observed in ALHA77307 and that may reflect the effect of secondary alteration processes on the parent body.

Kainsaz AOAs commonly show Fe enrichments at their edges. Individual olivine grains in most AOAs are rimmed by thin ferroan olivine veins, up to 3 μm in width, which tend to be restricted to olivine grain boundaries and preexisting cracks (Fig. 1). Similarly, Chizmadia et al.

(2002) observed the presence of abundant thin ferroan olivine veins rimming forsteritic olivine in AOAs from the CO3.2 chondrites Kainsaz, Rainbow, and Y82050. However, there are variations in the degree of Fe enrichments along the olivine grain boundaries between and within individual AOAs. For example, AOA 08 is partially rimmed by distinctly more FeO-rich, more equilibrated olivine (up to 5 μm in width) at one edge, while its interior and another edge show very narrow Fe enrichments up to 0.5 μm in width along olivine grain boundaries (Fig. 1a). Thick FeO-rich olivine rims appear rare, but most AOAs show similar widths of narrow ferroan olivine veins rimming forsteritic olivine grains throughout each inclusion (Figs. 1b-c). In addition, AOA 16 appears to consist of two separate inclusions (Fig. 2); one region contains all olivine grains with well-developed Fe enrichments along their rim, whereas another has olivine grains only in the outermost region that show Fe enrichments along their rim. This heterogeneous development of ferroan olivine veins along the olivine grain boundaries within and between individual AOAs has not been described before, probably due to the limited number of AOAs in CO3.2 chondrites studied by Chizmadia et al. (2002).

Overgrowths of very fine-grained, fibrous or platy ferroan olivine grains are sometimes heterogeneously developed on forsteritic olivine grains at the edges of AOAs (Figs. 3a-b). Occasionally, ferroan olivine overgrowths partially fill void space in the interior of AOAs (Fig. 3c). These overgrowth grains are usually elongated normal to the surface of the host olivine grains and vary in length with a range up to 5 μm. This variation can be observed from individual olivine grains that have thick overgrowths on one surface (i.e., favored in one crystallographic orientation), but very thin on the other (Fig. 3a). Many of the elongated ferroan olivine overgrowths on the same surfaces of the host olivine grains are aligned parallel to each other (Fig. 3b). There are sharp compositional boundaries between the ferroan olivine overgrowths and the host olivines, as indicated by abrupt contrast changes in BSE images. Bright, thin layers (≤0.5 μm in thickness) or fine grains (<1 μm in size) are often observed along these boundaries (Figs. 3b-c), suggesting the presence of high-Z materials (e.g., chromite).

Our electron microprobe analyses of olivine in Kainsaz AOAs show a compositional range of $Fa_{1.2\text{-}21.5}$ (Fig. 4; EA1). This range is consistent with that reported in Chizmadia et al. (2002), despite the larger number of measurements in this study. None of the analyses have compositions very close to forsteritic olivine composition (e.g., $Fa_{<1}$) that occur in ALHA77307 AOAs, probably due to our biased selection of the analyzed AOAs that contain well-developed

ferroan olivine veins and beam overlap between the cores and rims of olivine grains. Kainsaz AOA olivines contain TiO_2, Al_2O_3, Cr_2O_3, MnO, and Na_2O contents <1 wt%, which are similar to those in ALHA77307 AOAs. However, the majority of Kainsaz AOA olivines have Cr_2O_3 contents ≤0.1 wt% with a peak at 0-0.05 wt%, whereas most ALHA77307 AOA olivines have Cr_2O_3 contents ≥0.05 wt% with a peak at 0.1-0.15 wt% (Fig. 5). Such a reduced variability in Cr_2O_3 contents in AOA olivines with increasing petrologic subtype was also observed by Chizmadia et al. (2002). In addition, Kainsaz AOA olivines show a slightly wider range of MnO and Na_2O contents (Fig. 6). There is a close correlation between MnO and fayalite contents in Kainsaz AOA olivines, consistent with McSween (1977), but in contrast to ALHA77307 AOA olivines (Fig. 6a).

We were not able to obtain accurate electron microprobe measurements from ferroan olivine overgrowths on Kainsaz AOAs due to their fine-grained nature. Our SEM EDS analyses indicate that these ferroan olivine overgrowths are more FeO-rich ($Fa_{\sim 25\text{-}35}$) relative to the AOA interiors, but no pure or nearly endmember fayalite compositions were observed.

3.2. TEM observations of four Kainsaz AOAs

Olivine in the five FIB sections from four Kainsaz AOAs has common textural characteristics. Figure 7 is a mosaic of DF-STEM images showing representative textures of olivine grains from AOA 08. All FIB sections consist of dense aggregates of randomly-oriented olivine grains with straight or slightly curved grain boundaries and well-developed 120° triple junctions, indicating highly equilibrated textures. Minor pores and/or cracks are present in all FIB sections. The overall size of olivine grains is ~0.5-8.5 μm, mostly less than 5 μm, and each FIB section shows very similar ranges. Olivine grains have no evidence of strain and are almost free of defects.

Individual olivine grains are strongly zoned with a broad range of $Fa_{\sim 2\text{-}31}$; the fayalite content decreases rapidly over distances of <1 μm from the grain edges towards the interior and then is relatively constant towards their centers (Figs. 8, S1). Individual olivine grains within and between AOAs display different ranges of fayalite contents, but the degree of Fe enrichment generally increases towards the AOA peripheries. However, minor olivine grains with a size ≤ ~1 μm are uniformly Fe-enriched ($Fa_{\sim 20}$) from their core to rim. In comparison, ALHA77307 AOAs contain nearly pure forsterite only (i.e., $Fa_{<1}$ with mean $Fa_{0.1}$), as confirmed by previous

TEM studies (Han and Brearley, 2015, 2016).

At the edge of AOA 16, micron-sized, platy ferroan olivine grains form overgrowths on the host olivine grains, as indicated by BSE image (Fig. 2b). The interfaces between these two olivine grains are slightly curved and embayed toward the host olivine grains. We also observed ferroan olivine overgrowths, with a size up to ~400 nm, on forsteritic olivine grains at the edge of AOA 75, which were not detected by BSE imaging. Electron diffraction analyses and HRTEM imaging confirmed that both host olivine grains and ferroan olivine overgrowths are in crystallographic continuity. For example, in AOA 16, the ferroan olivine overgrows along the c axis, which shares the *c* direction of the underlying host olivine grain. The ferroan olivine overgrowths and the host olivines are compositionally distinct (Fig. 9), and the former has higher ranges of fayalite (Fa_{33-36}) and MnO (0.2-0.5 wt%) contents, relative to the latter that shows larger variations in both contents ($Fa_{<31}$, <0.3 wt% MnO). A good correlation between MnO and fayalite contents is observed from their host to overgrowth olivines. Similar compositional relationships were also observed from fayalitic overgrowths rimming isolated fosteritic olivine grains in matrix in carbonaceous and ordinary chondrites (e.g., Weinbruch et al., 1990; Weisberg et al., 1997; Weisberg and Prinz, 1998; Krot et al., 1997, 2000, 2004; Doyle et al., 2015; Simon et al., 2019).

3.2.1. Occurrence of chromite grains

Within all FIB sections, numerous chromite grains are found to be spatially associated with FeO-rich olivine in Kainsaz AOAs. The Fast Fourier Transform (FFT) analyses of their HRTEM images are consistent with the spinel structure. The chromite grains occur in four textural types (Figs. 10-13). First, abundant, elongated chromite nanoparticles ≤200 nm in size commonly decorate olivine grain boundaries (Figs. 10a-c) and occasionally crosscut olivine grains in the AOA interiors. The abundances of these nanoparticles generally increase towards the outer regions of the AOAs. The nanoparticles are all aligned along individual grain boundaries and share the same crystallographic orientation relationship with adjacent olivine: $a_{olivine}//(111)_{chromite}$, $b_{olivine}//[112]_{chromite}$, and $c_{olivine}//(110)_{chromite}$ (Figs. 10d-f). These crystallographically aligned nanoparticles, with Fe,Cr-bearing sulfide grains, also occur along the interfaces between the ferroan olivine overgrowths and the host AOA olivine grains (Fig. 11a) and correspond to the bright, thin layers or fine grains in BSE images (Figs. 3b-c).

Weisberg et al. (1997) also noted that, in matrix of the Krymka LL3.1 chondrite, bright, thin layers at the boundaries between fayalitic olivine overgrowths and forsteritic olivine substrates consist of chromite crystals in crystallographic alignment but did not report any specific orientation relationships between chromite and either of the olivines. Second, chromite lamellae, <0.1 μm in thickness and <1 μm in length, occur in ferroan olivine overgrowths at the AOA edge (Figs. 11a-b). They are elongated normal to the interfaces between the host olivine and ferroan olivine overgrowth and are oriented parallel to the c axis of the surrounding olivine overgrowth, as well as the AOA olivine because of the crystallographic continuity between these two olivines. Importantly, we found the same crystallographic orientation relationship from this occurrence of chromite with respect to olivine: $a_{olivine}$//$(111)_{chromite}$, $b_{olivine}$//$[112]_{chromite}$, and $c_{olivine}$//$(110)_{chromite}$ (Figs. 11c-f). Third, pores and cracks are partially filled with chromite grains that show various morphologies from rounded to elongated. Rarely, elongated chromite laths (<500 nm in length) grew into pores and are elongated normal to the exposed surfaces of olivine grains (Fig. 12). A set of the chromite laths along a single olivine grain boundary share their elongation direction with the c axis of underlying olivine. TEM EDX analyses indicate that these laths are surrounded by a thin layer of FeO-rich olivine. Finally, equant chromite grains ≤500 nm in size occur as inclusions in olivine grains, but no crystallographic orientation relationships between these two phases were observed (Fig. 13).

Analytical electron microscope analyses show a notable compositional variation between different textural types of chromite in Kainsaz AOAs. The thin, elongated chromite crystals, both in ferroan olivine overgrowths and in voids, are compositionally close to $FeCr_2O_4$, but only the grains in the overgrowths contain ≤3 wt% Al_2O_3. In contrast, the chromite grains along olivine grain boundaries and in olivine grains are $(Mg, Fe)(Al, Cr)_2O_4$ with variable amounts of Al_2O_3 and MgO. However, we were not able to determine the precise compositions, particularly the MgO and FeO contents, of these chromite grains due to their fine grain size and the considerable X-ray contributions from the host olivine. The X-ray peak intensities for Fe and Mg in TEM EDX spectra measured from the chromite grains along olivine grain boundaries and in olivine grains are different from those from the surrounding olivine, confirming the presence of both elements in them. There appear to be no detectable systematic variations in FeO contents in the chromite grains with distance from the AOA edge. In addition, olivine associated with the chromite grains contains uniformly low or no detectable Cr_2O_3 (≤0.2 wt%), and no detectable

Al_2O_3. Therefore, the varying intensities of X-ray peaks for Al and Cr in TEM EDX spectra result solely from the chromite grains along olivine grain boundaries and in olivine grains. Their Al_2O_3 contents appear to vary up to ~20 wt% where the grains occur near (altered) refractory Ca,Al-rich components, but in most cases contain ≤3 wt% Al_2O_3. We were able to determine atomic Cr/(Al+Cr) ratios of ~0.6-0.9 from three chromite inclusions (~200-350 nm in size) in olivine grains. However, the chromite nanoparticles (≤200 nm in size) along olivine grain boundaries were too small to obtain reliable concentrations of Cr and Al.

4. DISCUSSION

Kainsaz AOAs show mineralogical and chemical characteristics that are distinctly different from ALHA77307 AOAs, as follows: (1) the ubiquitous presence of strongly zoned olivine grains with Fe enrichments near their rim and along cracks (Figs. 1-2, 8, S1); (2) the heterogeneous ranges of fayalite contents in individual olivine grains (Fig. 4); (3) the narrower range of Cr_2O_3 contents in olivine (Fig. 5); (4) the wider ranges of MnO and Na_2O contents in olivine (Fig. 6); (5) the correlation between MnO and FeO contents in olivine (Figs. 6a, 9); (6) the formation of FeO-rich olivine overgrowths on the edges and in the pores of AOAs (Figs. 3, 11); and (7) the presence of abundant chromite grains (Figs. 10-13). These observations can be interpreted as the combined and complex effects of metasomatism and metamorphism in the CO3 chondrite parent body environment where a fluid was capable of a mobilization of Si, Al, Cr, Fe, and Mg, and, to lesser degrees, Mn and Na at relatively low temperatures (<500°C). In the following discussion, we examine in detail the conditions of metasomatism and metamorphism that affected the mineralogical and chemical evolution of Kainsaz AOAs.

4.1. Metamorphic effect on olivine in Kainsaz AOAs

The Fe enrichments in olivine at their rims, especially near the AOA edges, and along cracks are easily visible in BSE images (Figs. 1-2) and revealed in detail from compositional profiles determined by TEM EDX analysis (Figs. 8, S1). The Fe enrichments in olivine described in CO3 chondrites have been interpreted as indicators of Fe^{2+}-Mg^{2+} diffusive exchange between matrix and other components during thermal metamorphism (McSween, 1977; Scott and Jones, 1990; Chizmadia et al., 2002; Grossman and Brearley, 2005; Bonal et al., 2007; Imae and Nakamuta, 2018). This diffusion process appears to be widespread and affected AOAs as well as

other silicate components throughout the whole range of CO3 chondrite petrologic subtypes. However, the heterogeneous development of Fe enrichments between and within individual AOAs in Kainsaz (Figs. 1-2) indicates that there were highly localized variations in the degree of compositional equilibration in olivines. In particular, olivine grains on the AOA edges show a higher degree of Fe enrichment along their rims, compared to those in the interiors, and some AOAs are rarely surrounded by a more equilibrated, FeO-rich olivine rim (Fig. 1a), implying that the degree of equilibration depends on distance from the edge of AOAs, where Fe started to diffuse in from the matrix. A significant variability in olivine compositions within and between AOAs and chondrules was observed even in CO3 chondrites of the highest petrologic subtypes (e.g., Scott and Jones, 1990; Chizmadia et al., 2002). This suggests that complete compositional equilibration during thermal metamorphism was never achieved in the CO3 chondrite parent body, although equilibrium appears to have been approached on a local scale, and that AOAs in Kainsaz have not lost their primary nebular signatures completely due to thermal metamorphism.

4.2. Diffusion modeling for olivine thermal history

We carried out Fe^{2+}-Mg^{2+} interdiffusion modeling for olivine equilibration to constrain the metamorphic history necessary to produce the zoning profiles observed from AOA olivines in Kainsaz. Our modeling approach is similar to that used by Jones and Rubie (1991) and presented in detail in EA2. In this study, four olivine components were considered (Table S1): (1) AOA olivine with minor diopside, (2) type I chondrule olivine with or without a low-Ca pyroxene rim, (3) type II chondrule olivine, and (4) fine-grained matrix olivine. We used the zoning profiles of chondrule olivines measured from ALHA77307 by Jones and Rubie (1991), which represent the initial, un-metamorphosed compositions, and from Kainsaz by Schwinger et al. (2016). The CO3 chondrite parent body was assumed to have cooled for 2-3 Ma (e.g., Doyle et al., 2015) from a peak metamorphic temperature of ~500°C (Jones and Rubie, 1991; Busemann et al., 2007; Cody et al., 2008; Schwinger et al., 2016; Imae and Nakamuta, 2018) down to 300°C below which no more effective diffusion occurs. Our results are in good agreement with previous modeling results of the zoning profiles observed from chondrule olivines (Jones and Rubie, 1991; Schwinger et al., 2016) and can therefore be applied to those obtained from olivines in Kainsaz AOAs for this study. The calculated zoning profiles of olivines are shown in Figures 14-15.

4.2.1. Olivine in chondrules and matrix

Our diffusion calculations for the chemical evolution of olivine in chondrules and matrix during thermal metamorphism are in general agreement with previous studies (Jones and Rubie, 1991; Schwinger et al., 2016). Our models demonstrate that type I chondrule olivine experiences a larger extent of Fe-Mg interdiffusion (Fig. 14a), when it is assumed to be in direct contact with FeO-rich olivine in matrix and type II chondrules during thermal metamorphism. The calculated diffusion depth for type I chondrule olivine is much thicker and its rim composition is more FeO-rich, compared to profiles observed in any metamorphosed CO3 chondrites including Kainsaz. However, type I chondrule olivine in Kainsaz shows only a minor compositional modification at its edge in comparison with that in ALHA77307 (Scott and Jones, 1990; Jones and Rubie, 1991; Schwinger et al., 2016). This discrepancy was thoroughly examined by Jones and Rubie (1991), and they concluded that a pyroxene rim on type I chondrule olivine played an important role in limiting the extent of Fe-Mg interdiffusion in olivine between type I chondrule and matrix. Generally, olivine is poikilitically enclosed by pyroxene in type I chondrules from Kainsaz (Wick and Jones, 2012) so that Fe-Mg interdiffusion in type I chondrule olivine may have been affected by surrounding pyroxene whose Fe-Mg interdiffusion is very sluggish (Dohmen et al., 2016). Similar to Jones and Rubie (1991), we therefore assumed a fast diffusion pathway along fractures in the pyroxene rim on type I chondrule olivine and the total effective bulk diffusion coefficient of pyroxene to be 1.5× that of olivine lattice diffusivity. The calculated profile with the effect of the presence of the pyroxene rim is consistent with the observed profile of type I chondrule olivine from Kainsaz (Fig. 14b).

Type II chondrules do not have pyroxene rims and therefore compositional exchange occurs by diffusion directly between ferroan olivine phenocryst and matrix during thermal metamorphism. Our model matches well with diffusion profiles typically observed in type II chondrule olivines from Kainsaz (Fig. 14c), reported in Schwinger et al. (2016). Fayalite contents in matrix olivine decrease from Fa_{58} to $Fa_{\sim 50}$ (Fig. 14d), consistent with those reported from Kainsaz ($Fa_{\sim 20\text{-}55}$; Keller and Buseck, 1990; Brearley and Jones, 1998). In addition, a minimal compositional change in pyroxene in type I chondrule from Kainsaz is expected, due to its very sluggish Fe-Mg diffusivity (Dohmen et al., 2016).

4.2.2. AOA olivine

Our diffusion calculations that successfully match the profiles measured in type I and II chondrule olivines fail to reproduce the observed U-shaped zoning profile in Kainsaz AOA olivines. Instead, the calculations predict that AOA olivine is completely equilibrated at $Fa_{\sim 50}$ with surrounding matrix olivine, producing a flat profile (Fig. 15a). Highly elevated and uniform Fe contents are rarely observed in olivine grains ($Fa_{\sim 20}$) with a size ≤ ~1 μm and from highly equilibrated olivine grains ($Fa_{\sim 26}$) on the AOA exteriors (Fig. 1a). However, none of them have Fe contents as high as the matrix olivine. Our modeling results are also inconsistent with the observations of Chizmadia et al. (2002) who reported a range of olivine compositions in AOAs throughout petrologic subtypes from 3.2 to 3.7. Only the subtype CO3.8 chondrite Isna has equilibrated olivine compositions with a narrow range of $Fa_{64\text{-}67}$. Diopside in AOAs occurs enclosed by olivine and thus may have undergone Fe-Mg exchange with surrounding olivine only if the Fe diffuses far enough into the olivine. In the modeled diffusion profiles, only a slight Fe enrichment over a distance <0.1 μm from the edge of diopside is observed (Fig. 15b), because of the very slow Fe-Mg diffusivity in diopside (Müller et al., 2013). Collectively, olivine compositions in Kainsaz AOAs are very difficult to reconcile with a simple diffusional exchange process induced by a global metamorphic heating and subsequent cooling history, which is a feasible model for olivine zoning profiles measured from Kainsaz chondrules.

The discrepancy between the modeled diffusion profiles and those observed from olivines in Kainsaz AOAs, as well as the difference in olivine zoning profiles between chondrules and AOAs, suggest that the AOAs experienced different processes during peak thermal metamorphism that limited the ability of Fe to diffuse into the AOA olivine grains. The compact olivine grain boundaries in AOAs (Fig. 7; Han and Brearley, 2015) may have reduced the extent to which Fe diffused into the interior of olivine grains. On the other hand, with low-temperature metamorphic heating, olivine grains may have coarsened very slightly while pores became less abundant and larger, developing a higher degree of textural equilibrium (Karato, 1989). However, no apparent difference in AOA olivine grain sizes was observed between ALHA77307 and Kainsaz (see Section 4.3). To explain this puzzle, extensive analyses throughout petrologic subtypes from 3.0 to 3.8 are required to determine any systematic variations in olivine zoning pattern and composition and size distribution of olivine grains and pores in AOAs with increasing degree of thermal metamorphism.

We propose a two-stage alteration scenario to produce the pronounced zoning profiles observed from olivine grains in Kainsaz AOAs. During the peak of thermal metamorphism, primary forsteritic olivine grains ($Fa_{<1}$) in AOAs may have completely equilibrated at $Fa_{\sim 5\text{-}10}$ (solid line in Fig. 15c), by a volume diffusion of Fe into the center of olivine grains. On cooling after peak thermal metamorphism, a subsequent Fe-Mg exchange continued to occur along olivine grain boundaries, but was limited by slower diffusion rates at lower temperatures, forming a steep increase in Fe contents (up to $Fa_{\sim 31}$) at the edge of AOA olivine grains (dotted line in Fig. 15c). This late-stage diffusion process may have occurred in the presence of fluids, probably before the formation of FeO-rich olivine overgrowths onto the exterior of AOA olivines (Figs. 3, 11) and numerous chromite grains along olivine grain boundaries and within olivine grains (Figs. 10-13). Under this two-stage alteration scenario, we produced the best fit with the observed zoning profile of AOA olivines in Kainsaz (Figs. 8, S1), having a forsteritic core ($Fa_{\sim 4\text{-}8}$) with a gradual Fe enrichment (up to $Fa_{\sim 27}$) towards the edge. A similar history may apply to AOA olivines in CO3 chondrites of higher petrologic types up to 3.6, which maintain their forsteritic cores ($Fa_{<\sim 10}$; Chizmadia et al., 2002).

We also modeled the zoning profiles of olivine at variable peak temperatures of hydrothermal alteration following the peak of thermal metamorphism at 500°C (Fig. 15d), considering that the presence of fluids was experimentally proven to enhance the Fe-Mg interdiffusion rates in olivine (Hier-Majumder et al., 2005; Costa and Chakraborty, 2008). On cooling from the peak temperature of 350°C, 20× faster Fe-Mg interdiffusivity under wet conditions than in under dry conditions is required to produce the zoning profiles obtained from Kainsaz AOA olivines. The cooling from the peak temperatures of 300°C and 200°C requires 1000 and 2×10^7 times faster Fe-Mg interdiffusivity in a wet condition, values which are far too high because the enhancement of Fe-Mg diffusion rates from dry to wet conditions is only by a factor of up to ~50 at 1100°C (Hier-Majumder et al., 2005). These calculations suggest that different degrees of Fe enrichments in a narrow zone (<1 μm) along olivine grain boundaries between and within Kainsaz AOAs could also be the result of relatively lower-temperature, short-lived events, possibly due to a limited availability of fluids on a local scale.

The thermal history proposed here for the zoned olivine grains in Kainsaz AOAs should also have affected chondrule olivines in the same meteorite. Schwinger et al. (2016) reported that compositional profiles measured by EPMA of chondrule olivines in Kainsaz show typical zoning

depths of ~20-40 μm. In contrast, zoning depths for AOA olivine grains determined by TEM EDX in this study are ~0.6 μm (Figs. 8, S1), which is difficult to resolve by EPMA. Similar short diffusion profiles may be present on the edges of chondrule olivines, but further chemical studies are required to confirm this.

4.3. Annealed texture of olivine in Kainsaz AOAs

Olivine grains in Kainsaz AOAs are characterized by highly equilibrated grain boundary textures (Fig. 7), identical to those observed from AOAs in ALHA77307 (Han and Brearley, 2015) and other carbonaceous chondrites (Komatsu et al., 2001). In addition, the grain size of AOA olivines shows a similar range for Kainsaz and ALHA77307, and most grains are less than 5 μm in size (0.5-6.5 μm for ALHA77307; Han and Brearley, 2015). Chizmadia et al. (2002) estimated a similar range of olivine grain size from 2 μm to 10 μm, based on BSE imaging of apparent developments of Fe enrichments along olivine grain boundaries in AOAs from CO3 chondrites of petrologic subtypes 3.3 to 3.5. Collectively, this consistency demonstrates that there is no systematic correlation of grain size and texture in AOAs with petrologic subtype in CO3 chondrites, i.e., no evidence for grain growth of the AOA olivines, and that all AOAs show highly equilibrated grain boundary textures. This is inconsistent with McSween (1977), who noted that AOAs become cloudy with increasing degree of alteration, indicative of textural recrystallization (Rubin, 1998). However, the cloudiness may, in fact, be the result of the formation of numerous chromite grains along olivine grain boundaries, as observed here in Kainsaz AOAs (Fig. 10). We therefore conclude that, even down to the TEM scale, Kainsaz AOAs show minimal effects of thermal metamorphism on their textures and preserve a high degree of textural equilibrium that formed by thermal annealing in the solar nebula (Komatsu et al., 2001; Han and Brearley, 2015).

4.4. Olivine overgrowths on Kainsaz AOAs

The presence of ferroan olivine overgrowths on olivine grains in refractory inclusions, chondrules, and matrices from carbonaceous chondrites, especially the oxidized CV3 Allende chondrite, has been widely reported (Brearley and Krot, 2013 and references listed therein). The ferroan olivine overgrowths observed from Kainsaz AOAs (Figs. 3, 11) are very comparable in texture, morphology, and composition to those in the oxidized CV3 chondrites, except for their

relatively smaller size and lower abundance. This similarity, coupled with evidence for the complete absence of ferroan olivine overgrowths on AOAs in ALHA77307 (Han and Brearley, 2015, 2016), suggests that the ferroan olivine overgrowths on Kainsaz AOAs formed by a similar process, i.e., low-temperature, fluid-assisted metamorphism on the parent body (Krot et al., 1997, 2000, 2004), but to lesser degrees. The crystallographic continuity along the c axis between the ferroan olivine overgrowth and the host olivine (Fig. 11a) is consistent with its low-temperature growth in the presence of a fluid, as demonstrated experimentally by Dobrică et al. (2022), and is evidence for direct epitaxial growth of ferroan olivine over primary AOA olivine. The elevated Mn concentrations in the ferroan olivine overgrowths on Kainsaz AOAs (Fig. 9) are also consistent with their precipitation from a fluid that had elevated activities of Mn (Krot et al., 2000, 2004; Zolotov et al., 2006). We therefore infer that Fe, Mg, Si, and Mn were dissolved and mobilized by an aqueous solution on the parent body and subsequently precipitated as secondary ferroan olivine onto primary AOA olivines. These elements were likely derived from amorphous silicates that constitute the matrix of the least altered, very low petrologic subtype CO3.0 chondrites, like ALHA77307 (Brearley, 1993) and DOM 08006 (Davidson et al., 2019). The heterogeneous occurrence of fine-grained ferroan olivine overgrowths on Kainsaz AOAs (Fig. 3) indicates that very limited and localized alteration did occur, which can be attributed to a limited availability of fluids (i.e., limited fluid-mineral interaction) on a local scale, as we suggest earlier in Section 4.2.2.

The observed sharp interfaces between the ferroan olivine overgrowths and the host AOA olivines (Figs. 3, 9, 11b) indicate minimal diffusional equilibration between these two olivines after the overgrowths formed (Krot et al., 2000; Imai and Yurimoto, 2003; Doyle et al., 2015; Simon et al., 2019). This implies that the ferroan olivine overgrowths formed late following the peak of metamorphism, when temperatures were too low to allow Fe-Mg interdiffusion, resulting in compositional disequilibrium between the ferroan olivine overgrowths and the host AOA olivines. In addition, the ferroan olivine overgrowths (Fa_{33-36}; Fig. 9) on Kainsaz AOAs are distinctly poorer in FeO contents than the matrix olivine ($Fa_{\sim 20-55}$; Keller and Buseck, 1990; Brearley and Jones, 1998), indicating also that they formed at low temperatures and were not able to equilibrate with the matrix that is much finer-grained**.** This conclusion is supported by recent equilibrium thermodynamic calculations in the water-chondrite system showing that fayalite (Fa_{88-100}) can form as a minor phase at temperatures below ~350°C and a water/rock ratio

of 0.06-0.2 (Zolotov et al., 2006; Jogo et al., 2009). The considerable MgO contents in the ferroan olivine overgrowths (Fig. 9) suggest that they formed at higher temperatures and/or lower water/rock ratios compared to those calculated for the formation of pure fayalite (Zolotov et al., 2006; Jogo et al., 2009). Thus, we conclude that the formation of ferroan olivine overgrowths on the Kainsaz AOAs was a late-stage disequilibrium process with a limited amount of fluid that occurred during the cooling history of the CO3 chondrite parent body, but at temperatures higher than those needed to stabilize phyllosilicates rather than grow ferroan olivine (and chromite grains).

4.5. Formation of chromite in Kainsaz AOAs

An important observation in this study is that abundant chromite grains are found along olivine grain boundaries, in olivine grains, and in voids between olivine grains from Kainsaz AOAs (Figs. 10-13). There are two main possible mechanisms for the formation of chromite in Kainsaz AOAs; (1) high-temperature condensation from a nebular gas (Weinbruch et al., 1990; Weisberg et al., 1997) and (2) low-temperature alteration on the parent body (Krot et al., 1997; Marinova et al., 2021).

The chromite grains in Kainsaz AOAs may have formed by condensation from a hot, highly oxidizing nebular gas. The condensation origin has been proposed largely based on the widespread occurrence of fayalitic olivine in the oxidized CV3 chondrites such as Allende (e.g., Hua et al., 1988; Palme and Fegley, 1990; Weinbruch et al., 1990; Weisberg and Prinz, 1998). However, Allende preserves strong lines of evidence for pervasive parent body alteration that affected all of its components (Brearley and Krot, 2013), and the formation of fayalitic olivine in Allende has been recognized to be the result of combined, complex effects of metasomatism and thermal metamorphism in an asteroidal setting (e.g., Krot et al., 1997, 2000, 2004; Zolotov et al., 2006; Jogo et al., 2009; Doyle et al., 2015). In addition, thermodynamic equilibrium calculations show that condensation from a gas, even under conditions with highly enhanced dust/gas ratios, only form olivine with relatively low fayalite contents (i.e., $Fa_{14.5}$; Fedkin and Grossman, 2006). Thus, the Fe enrichments along olivine grain boundaries in Kainsaz AOAs cannot be explained by condensation from an oxidizing nebular gas, implying that condensation of gaseous Fe and Cr into chromite is also unlikely.

Conclusive evidence against the condensation origin of chromite in Kainsaz AOAs is

provided by a comparison with AOAs from the primitive chondrites of petrologic subtype 3.0, for example, ALHA77307 (e.g., Scott and Jones, 1990; Grossman and Brearley, 2005; Bonal et al., 2007; Kimura et al., 2008). Han and Brearley (2015, 2016) studied a total of 179 AOAs in ALHA77307 using a field emission SEM and seven AOAs using TEM, and did not find any similar types of chromite. In contrast, chromite is present in each of the Kainsaz AOAs we studied using TEM. The complete absence of such chromite in ALHA77307 AOAs therefore supports the view that its occurrence in Kainsaz AOAs are the products of secondary parent body processes and is further evidence for the mobilization and redistribution of Cr with Fe during such processes. Importantly, Kainsaz AOAs contain the four textural types of chromite grains that show differences in composition and crystallographic orientation relationship with respect to adjacent olivine (Figs. 10-13). These observations indicate distinct formation conditions, possibly different sources of Fe, Cr, and Al, for the formation of each type of chromite, although they may have all formed contemporaneously. We now consider how each of these four different textural types formed on the parent body.

4.5.1. Chromite nanoparticles along olivine grain boundaries

Abundant chromite nanoparticles occur along olivine grain boundaries and have the crystallographic orientation relationship with adjacent olivine, i.e., $[110]_{chromite}//[001]_{olivine}$ and $(111)_{chromite}//(100)_{olivine}$ (Fig. 10). This is a classic orientation relationship between a spinel-structured phase and olivine for solid state exsolution processes (Champness, 1970). The same relationships were observed from chromite inclusions in olivine from metamorphosed H chondrites of petrologic types 4 to 6 (Ashworth, 1979), from a chromite-rich vein in a chondrule olivine grain in Allende (Weinbruch et al., 1990), and from Cr-rich platelets as a magnetite-chromite-spinel solid solution in the Allende matrix olivine grains (Marinova et al., 2021). These observations were also interpreted as evidence for exsolution of chromite by *in situ* oxidation of olivine at moderate temperatures (<800°C; Champness, 1970).

A key question is the source of Cr, Fe, and Al to form these chromite nanoparticles associated with olivine in Kainsaz AOAs. A consideration of the compositional constraints suggests that two types of olivines in AOAs are a viable internal source of Cr: (1) primary forsteritic olivines that formed as high-temperature nebular condensates or (2) Cr-rich, ferroan olivine that formed during thermal metamorphism. It is also possible that Cr was externally

559 derived from chondrule olivines, particularly type IIA chondrules (e.g., Grossman and Brearley,
560 2005), and matrix. The matrix is most likely a source of Fe, whereas Al may have been
561 mobilized during alteration of refractory Ca,Al-rich phases in AOAs.
562 It is possible that Cr could have been entirely derived from primary forsteritic olivines in
563 AOAs with the onset of thermal metamorphism. Figure 5 shows that the majority of olivines in
564 Kainsaz AOAs have Cr_2O_3 contents ≤0.1 wt% with a peak at 0-0.05 wt%, whereas most
565 ALHA77307 AOA olivines have Cr_2O_3 contents ≥0.05 wt% with a peak at 0.1-0.15 wt%. This
566 compositional difference suggests that Cr was lost from AOA olivines during thermal
567 metamorphism (Chizmadia et al., 2002). Scott and Jones (1990) and Grossman and Brearley
568 (2005) also demonstrated that Cr is easily lost from olivine in type IIA chondrules with the onset
569 of thermal metamorphism. It is therefore possible that, during thermal metamorphism, Cr was
570 lost from the primary AOA olivines and concentrated on the grain boundaries as an exsolved
571 chromite phase. However, an external source of all Fe is required, probably from the surrounding
572 matrix (Chizmadia et al., 2002), because ALHA77307 AOA olivines are nearly pure forsterite
573 (Fig. 4), consistent with previous TEM EDX analyses that showed that they contain <0.3 wt%
574 FeO (Han and Brearley, 2015, 2016).
575 Alternatively, the chromite nanoparticles in Kainsaz AOAs may have formed by a two-
576 stage process that is entirely the result of parent body thermal metamorphism. The first stage
577 involves that formation of Cr-rich ferroan olivine by diffusion of Fe and Cr into the edges of
578 primary forsteritic AOA olivines during the prograde thermal metamorphic path. The second
579 stage involves exsolution of the Cr and Fe from the secondary ferroan olivine during cooling,
580 following the peak of thermal metamorphism. However, this hypothesis seems unlikely, because
581 Cr is lost very rapidly from olivines in both AOAs (Fig. 5; Chizmadia et al., 2002) and
582 chondrules (Scott and Jones, 1990; Grossman and Brearley, 2005) in the early stages of thermal
583 metamorphism, so that Cr is not expected to have been retained or regained in olivine in AOAs
584 during asteroidal heating.
585 Instead, all or some Cr with all Fe could have been derived from an external source such
586 as chondrules and matrix, possibly transported by a fluid into the AOAs. It is plausible that
587 during thermal metamorphism, these elements were mobile along the olivine grain boundaries,
588 but were not readily incorporated into the olivine, and consequently nanometer-sized chromite
589 grew as individual, isolated grains in an epitaxial relationship with the host olivine. This scenario

is supported by the observed decrease in the abundance of chromite nanoparticles in AOAs with increasing distance from the surrounding matrix.

Kimura et al. (2006) argued that Cr in chromite from the matrix of LL3.00-3.3 chondrites could have been derived from oxidation of Fe,Ni metal during metamorphism, based on the observations that minor Cr is present in Fe,Ni metal in the least altered, pristine chondrites Semarkona (LL3.00), ALHA77307, and Acfer 094 (CC ungrouped) (Kimura et al., 2008). Scott and Jones (1990) showed that kamacite in ALHA77307 chondrules contains the highest mean levels of Cr and that Cr concentrations in kamacite systematically decrease with increasing metamorphic sequence of CO3 chondrites (McSween, 1977). However, Kimura et al. (2008) noted that Cr contents of Fe,Ni metal in chondrules and matrix in Semarkona and Acfer 094 generally overlap with those in CO chondrites of subtypes 3.03-3.1, in contrast to Y791717 (CO3.6) metals which contain much lower concentrations of Cr. It seems likely that only minor Cr was derived externally from Fe,Ni metal in chondrules and matrix in Kainsaz, with most being still retained in them due to low-temperature metamorphic heating. Fe,Ni metal is also common in AOAs (e.g., Han and Brearley, 2015) so can be a potential internal source of Cr. However, any systematic studies of AOA metals are lacking. A detailed chemical study throughout the CO3 chondrite petrologic subtypes 3.0 to 3.8 is thus required to better understand a behavior of Cr in AOA metals in response to thermal metamorphism.

All the Al required to form Al-bearing chromite cannot have been derived from any type of AOA olivines because their Al_2O_3 contents both in ALHA77307 and Kainsaz are overlapping ($\leq$0.6 wt%; EA1). In particular, TEM EDX analyses show no detectable Al contents in Kainsaz AOA olivines that contain Al-bearing chromite nanoparticles. Brearley and Jones (1998) found a similar behavior for Al_2O_3 contents of chondrule olivines from CO3 chondrites, which are essentially identical in ALHA77307 and metamorphosed CO3.1-3.7 chondrites. These data indicate that the Al_2O_3 contents of olivine in AOAs and chondrules have not been affected significantly by thermal metamorphism. Experimental studies showed that Al diffusion in olivine is very slow even at high temperatures and/or pressures (Jurewicz and Watson, 1988; Spandler et al., 2007; Spandler and O'Neill, 2010), probably due to a coupled substitution of Al for Mg in the octahedral site and for Si in the tetrahedral site (Evans et al., 2008). Spandler and O'Neill (2010) indicated that diffusion rates of Al in olivine ($D_{Al} < 10^{-17}$ m^2/s) are at least two orders of magnitude slower than those of divalent cations such as Fe^{2+} and Mg^{2+} at 1300°C (Spandler et

al., 2007). Peak metamorphic temperatures for Kainsaz are unlikely to have been much higher than 500°C (Jones and Rubie, 1991; Busemann et al., 2007; Cody et al., 2008; Schwinder et al., 2016; Imae and Nakamuta, 2018), too low to produce any detectable diffusion of Al, even over extended periods of time. It is therefore very problematic that Al diffused in and out both of the host forsteritic and ferroan olivine grains during thermal metamorphism.

On the other hand, the observed higher Al_2O_3 contents in the chromite nanoparticles in close proximity to refractory Ca,Al-rich components in Kainsaz AOAs suggest that Al was mobilized from these components, selectively melilite and anorthite. Based on the good correlation between mineralogy and alteration degree from Al-rich inclusions in AOAs from Allende, Hashimoto and Grossman (1987) found that melilite was the first primary phase to disappear during alteration, followed by Al,Ti-rich diopside and spinel; all three phases were progressively replaced to form secondary alteration assemblages including phyllosilicates by reacting with alkali-rich fluids. Although there has been no comprehensive study of alteration of refractory Ca,Al-rich components in AOAs in CO3 chondrites, Kojima et al. (1995) observed that the abundance of anorthite in AOAs decreases with increasing metamorphic grade, instead nepheline becomes abundant, suggesting that anorthite was replaced by nepheline during thermal metamorphism. Rubin (1998) reported the occurrence of small veins of nepheline in AOAs that replaced primary melilite during hydrothermal alteration. In addition, the preferential replacement of primary melilite and anorthite to various degrees by nepheline is evident in CAIs in Kainsaz and other CO3 chondrites of similar petrologic subtypes, indicative of widespread metasomatic alteration of these phases by interaction with fluids on the parent body (e.g., Tomeoka et al., 1992; Kojima et al., 1995; Russell et al., 1998; Wasson et al., 2001; Itoh et al., 2004). Previous hydrothermal experiments performed at 200-400°C for 7 days demonstrated that melilite and anorthite were dissolved readily by a fluid to release Al, Si, and Ca, forming hydrous phases such as Na zeolite (Nomura and Miyamoto, 1998; Ichimura et al., 2017). Thus, it is possible that Al was lost and transported in the presence of fluids at the earliest stages of metasomatic alteration of melilite and anorthite in Kainsaz AOAs and subsequently incorporated into Al-bearing chromite nanoparticles.

Overall, it is possible that neither of these two mechanisms, exsolution and epitaxial growth, is mutually exclusive. Some elements may be exsolved from the primary AOA olivines and some may have come from outside the AOAs. It is certain that the Fe in the chromite

nanoparticles was externally derived by grain boundary diffusion, possibly with the aid of a fluid, and the Al was very likely to be derived from metasomatic alteration of primary melilite and anorthite in refractory Ca,Al-rich components within the AOAs. Chromium lost from the AOA forsteritic olivines during the early stages of thermal metamorphism could reasonably be the primary source of Cr in the chromite nanoparticles. However, the abundance of chromite nanoparticles decreases with increasing distance from the surrounding matrix, suggesting that they preferentially formed along olivine grain boundaries in the outermost part of AOAs where Fe and some of Cr started to diffuse in from an external source (i.e., matrix). The chromite nanoparticles are absent on some of olivine grain boundaries even within the same FIB sections, suggesting that their formation occurred heterogeneously on surfaces of olivine grains with the appropriate atomic structure due to their crystallographic orientation to allow epitaxial nucleation and growth.

4.5.2. Chromite lamellae in olivine overgrowths

All of the chromite lamellae in ferroan olivine overgrowths share the same crystallographic orientation relationship with the surrounding olivine overgrowths (Fig. 11). This suggests that the chromite lamellae formed by exsolution or epitaxial growth, as discussed in Section 4.5.1. First, the chromite lamellae may have exsolved from the surrounding ferroan olivine overgrowths after their precipitation from a Fe-rich fluid onto the AOA exteriors (e.g., Krot et al., 1997, 2000, 2004; Zolotov et al., 2006; Jogo et al., 2009; Doyle et al., 2015). However, this is unlikely due to the high abundance of chromite lamellae in ferroan olivine overgrowths, which requires too much Cr to have exsolved from the overgrowths. In addition, as discussed in Section 4.4, the ferroan olivine overgrowths onto the host AOAs formed at temperatures that were too low to permit Fe-Mg diffusion between the overgrowth and the AOA forsteritic olivine substrate. Such conditions probably preclude the exsolution of Cr and Fe from the ferroan olivine overgrowths as a mechanism to form the chromite lamellae. Alternatively, the chromite lamellae may have nucleated and grew epitaxially simultaneously with ferroan olivine overgrowths, as Cr was lost from olivine in AOAs (and chondrules) and mobilized together with Fe during thermal metamorphism. It is also possible that the chromite lamellae began to overgrow on the AOA edges and were then overgrown by ferroan olivine in an epitaxial relationship, like those in the voids between olivine grains (Figs. 12b-c).

4.5.3. Chromite grains in voids

The common occurrence of chromite grains in voids between olivine grains can be attributed to the mobilization of Cr and Fe by an aqueous solution and subsequent precipitation of secondary chromite in the voids during cooling. Especially, many chromite grains are elongated normal to the edges of olivine grains, and some are aligned along the c axis of underlying olivine (Fig. 12a). These observations indicate their epitaxial nucleation and growth onto the exposed surfaces of olivine. The occurrence of a thin FeO-rich olivine coating on the chromite laths (Fig. 12c) may be a thin layer that formed after chromite, as an initial precipitate of ferroan olivine overgrowth. In addition, the chromite nanoparticles occur along the edges of olivine grains forming voids (Fig. 12b), which may represent the earliest stages of nucleation of numerous elongated chromite laths onto the exposed surfaces of olivine grains.

4.5.4. Chromite inclusions in olivine grains

Equant chromite grains are distributed throughout olivine grains in Kainsaz AOAs (Fig. 13). Similarly, Grossman and Brearley (2005) observed equant chromite inclusions in type II chondrule olivine in ordinary chondrites of petrologic subtype ≥3.3, in contrast to olivine in ordinary chondrites of petrologic subtypes 3.1-3.2 that contains fine, needle-like chromite aligned along preferred crystallographic directions. They argued that thermal metamorphism enabled homogeneous nucleation of fine chromite precipitates in olivine and subsequent prolonged heating resulted in the coarsening of the precipitates to much larger, equant chromite grains in olivine (Ashworth, 1979). Kainsaz appears to have experienced a similar degree of thermal metamorphism to ordinary chondrites of petrologic subtype ≥3.2 (Grossman and Brearley, 2005). Thus, the chromite inclusions in olivine in Kainsaz AOAs may have experienced a similar formation history in which chromite began to be exsolved from fosteritic olivine with the onset of thermal metamorphism and, with continuing heating, grew into sub-micrometer-sized, equant chromite grains. However, AOA forsteritic olivine grains from CO3.0 chondrites have very low Fe contents ($Fa_{\leq 1}$; Chizmadia et al., 2002; Han and Brearley, 2015, 2016), so any Fe had to be introduced into the olivine grains by a volume diffusion from the surrounding matrix, in order to drive exsolution of chromite grains. It is likely that Al was derived from metasomatic alteration of primary melilite and anorthite in the AOAs.

4.6. Implications on alteration conditions

Overall, the observed textural varieties of chromite grains in Kainsaz AOAs provide evidence for a mobilization of Al, Cr, and Fe along olivine grain boundaries and into olivine grains probably with the aid of an aqueous solution at lower temperatures following the peak of thermal metamorphism. Their formation was mostly the result of crystallographically-controlled processes, including exsolution, epitaxial growth, or a combination. These processes were favored in the crystallographic orientation relationship observed in this study (Figs. 10-12), such as $[110]_{chromite}//[001]_{olivine}$ and $(111)_{chromite}//(100)_{olivine}$. In addition, an epitaxial overgrowth of ferroan olivine was favored in the crystallographic orientation relationship, i.e., along the c axis of olivine (Fig. 11a).

The survival of small chromite grains (mostly <500 nm) in Kainsaz AOAs indicates that they must have formed in the late stages of thermal metamorphism after peak metamorphic conditions. Otherwise, they would have undergone coarsening to form larger particles during an asteroidal heating after their formation. Our interpretation is supported by important TEM observations of ferroan olivine overgrowths on Kainsaz AOAs: (1) the heterogeneous occurrence of fine-grained overgrowths (Fig. 3); (2) the observed distinct compositional difference between the overgrowths and the host AOA olivines (Figs. 9, 11b); and (3) the significant compositional difference between the overgrowths (Fa_{33-36}; Fig. 9) and the matrix olivine ($Fa_{\sim 20-55}$; Keller and Buseck, 1990; Brearley and Jones, 1998). These observations attest to little or no Fe^{2+}-Mg^{2+} interdiffusion in olivine grains between different components after overgrowth of ferroan olivine on the AOA exteriors. They would certainly have undergone Fe-Mg exchange and equilibrated with the matrix olivines if the ferroan olivine overgrowths formed during the early stage of thermal metamorphism when temperature was increasing. Therefore, the formation of ferroan olivine overgrowths and chromite grains clearly had to be a late-stage, fluid-driven process that occurred at relatively lower temperatures (<500°C), following the peak of thermal metamorphism.

5. CONCLUSIONS

Our TEM analyses of AOAs from Kainsaz (CO3.2) provide new insights into complex secondary asteroidal processes that modified the primary nebular features of AOAs as a response

to thermal metamorphism. This study offers strong lines of evidence for the mobilization of Fe, Mg, Si, Cr, and Al and their incorporation into secondary alteration phases in the presence of fluids during the thermal history on the CO3 chondrite parent body, as illustrated in Figure 16.

The prominent characteristic of Kainsaz AOAs is strongly zoned olivine grains with heterogeneous Fe enrichments along their grain boundaries, compared to ALHA77307 AOAs. This observation is widely interpreted as a result of Fe^{2+}-Mg^{2+} diffusional exchange with the surrounding matrix during metamorphic heating. Our diffusion calculations show that such olivine zoning and compositions cannot be produced during a global metamorphic history, which is a feasible model for the chondrule olivine zoning profiles observed from Kainsaz. The two-stage scenario is proposed for the Kainsaz AOAs, involving an initial equilibration at $Fa_{\sim 4\text{-}8}$ during peak metamorphic heating, when Fe diffused into the center of forsteritic olivine grains, followed by steep Fe enrichments up to $Fa_{\sim 20\text{-}27}$ along the edge of olivine grains. This late-stage diffusion may have occurred in the presence of limited fluids, resulting in different extents of Fe-Mg interdiffusion along indviduial olivine grain boundaries.

In Kainsaz AOAs, fine-grained ferroan olivine overgrowths occur heterogeneously in crystallographic continuity with olivines on the edges of the AOAs, and occasionally into pore spaces between olivine grains in the interiors. These overgrowths have compositionally sharp interfaces with the host AOA olivines, and they are more FeO-rich than the underlying AOA olivines, but less FeO-rich than the surrounding matrix. These observations indicate that the ferroan olivine overgrowths formed by precipitation from fluids in an epitaxial relationship onto the AOA exteriors. In addition, numerous chromite grains are found along olivine grain boundaries, in olivine grains, and in voids between olivine grains from Kainsaz AOAs. Different textural types of chromite share the similar crystallographic orientation relationships with adjacent olivine, suggesting that they formed by exsolution, epitaxial growth, or combined. We infer that Cr was primarily derived from AOA forsteritic olivines and less from chondrules, but all Fe were derived externally from the surround matrix, while Al was released during hydrothermal alteration of Ca,Al-rich components in the AOAs. Collectively, we conclude that the formation of ferroan olivine overgrowths and chromite grains was a crystallographically-controlled, fluid-driven process in the late stages of parent body thermal history, following the peak of thermal metamorphism. This process likely occurred at relatively lower temperatures (<500°C), probably following the full development of strongly zoned olivine grains in the

776 AOAs.
777
778 **ACKNOWLEDGEMENTS**
779 This work was supported by NASA grants EW14-2-122 (JH) and NNX15AD28G (AJB);
780 and KOPRI grant PE22050 (CP). We gratefully acknowledge the access to the Electron
781 Microbeam Analysis Facility at Department of Earth and Planetary Sciences and Institute of
782 Meteoritics, University of New Mexico and at Astromaterials Research and Exploration Science
783 Division, NASA Johnson Space Center. We thank Dr. Kimura and an anonymous reviewer for
784 their reviews and Dr. Krot for his editorial handling. LPI contribution xxxx. LPI is operated by
785 USRA under a cooperative agreement with the Science Mission Directorate of the National
786 Aeronautics and Space Administration.
787
788 **APPENDIX A. SUPPLEMENTARY MATERIAL**
789 **EA1.** Chemical compositions of olivine in amoeboid olivine aggregates from the ALHA77307
790 CO3.0 and Kainsaz CO3.2 chondrites, determined using electron microprobe and TEM EDX.
791 **EA2.** Diffusion modeling of zoned olivine grains in Kainsaz AOAs.
792

REFERENCES

Ashworth J. R. (1979) Two kinds of exsolution in chondritic olivine. *Mineral. Mag.* **43**, 535–538.

Bonal L., Bourot-Denise M., Quirico E., Montagnac G. and Lewin E. (2007) Organic matter and metamorphic history of CO chondrites. *Geochim. Cosmochim. Acta* **71**, 1605–1623.

Brearley A. J. (1993) Matrix and fine-grained rims in the unequilibrated CO3 chondrite, ALHA77307: Origins and evidence for diverse, primitive nebular dust components. *Geochim. Cosmochim. Acta* **57**, 1521–1550.

Brearley A. J. and Jones R. H. (1998) Chondritic meteorites. In *Reviews in Mineralogy, Volume 36, Planetary Materials* (ed. J. J. Papike), pp. 3-001–3-398.

Brearley A. J. and Krot A. N. (2013) Metasomatism in the early solar system: The record from chondritic meteorites. In *Metasomatism and the Chemical Transformation of Rock. Lecture Notes in Earth System Sciences*. Springer, Berlin, Heidelberg, pp. 659–789.

Busemann H., Alexander C. M. O'D. and Nittler L. R. (2007) Characterization of insoluble organic matter in primitive meteorites by microRaman spectroscopy. *Meteorit. Planet. Sci.* **42**, 1387–1416.

Champness P. E. (1970) Nucleation and growth of iron oxides in olivines. *Mineral. Mag.* **37**, 790–800.

Chizmadia L. J., Rubin A. E. and Wasson J. T. (2002) Mineralogy and petrology of amoeboid olivine inclusions in CO3 chondrites: Relationship to parent-body aqueous alteration. *Meteorit. Planet. Sci.* **37**, 1781–1796.

Cody G. D., Alexander C. M. O'D., Yabuta H., Kilcoyne A. L. D., Araki T., Ade H., Dera R., Fogel M., Militzer B. and Mysen B. O. (2008) Organic thermometry for chondritic parent bodies. *Earth Planet. Sci. Lett.* **272**, 446–455.

Davidson J., Alexander C. M. O'D., Stroud R. M., Busemann H. and Nittler L. R. (2019) Mineralogy and petrology of Dominion Range 08006: A very primitive CO3 carbonaceous chondrite. *Geochim. Cosmochim. Acta* **265**, 259–278.

Dobrică E., Nuth J. A. and Brearley A. J. (20221) Fayalite formation through hydrothermal experiments: Insights into early fluid-assisted hydration processes on asteroids. *Meteorit. Planet. Sci.* https://doi.org/10.1111/maps.13765.

Dohmen R., Ter Heege J. H., Becker H.-W. and Chakraborty S. (2016) Fe-Mg interdiffusion in

orthopyroxene. *Am. Miner.* **101**, 2210-2221.

Doyle P. M., Jogo K., Nagashima K., Krot A. N., Wakita S., Ciesla F. J. and Hutcheon I. D. (2015) Early aqueous activity on the carbonaceous and ordinary chondrite parent asteroids recorded by secondary fayalite. *Nat. Comm.* **6**, 1–10.

Evans T. M., O'Neill H. St. C. and Tuff J. (2008) The influence of melt composition on the partitioning of REEs, Y, Sc, Zr and Al between forsterite and melt in the system CMAS. *Geochim. Cosmochim. Acta* **72**, 5708–5721.

Fagan T. J., Krot A. N., Keil K. and Yurimoto H. (2004) Oxygen isotopic evolution of amoeboid olivine aggregates in the reduced CV3 chondrites Efremovka, Vigarano, and Leoville. *Geochim. Cosmochim. Acta* **68**, 2591–2611.

Fedkin A. V. and Grossman L. (2006) The fayalite content of chondritic olivine: Obstacle to understanding the condensation of rocky material. In *Meteorites and the early solar system II* (eds. D. Lauretta and H. Y. McSween). Arizona University Press, Tucson, pp. 279–294.

Grossman J. N. and Brearley A. J. (2005) The onset of metamorphism in ordinary and carbonaceous chondrites. *Meteorit. Planet. Sci.* **40,** 87–122.

Han J. and Brearley A. J. (2015) Microstructural evidence for complex formation histories of amoeboid olivine aggregates from the ALHA77307 CO3.0 chondrite. *Meteorit. Planet. Sci.* **50**, 904–925.

Han J. and Brearley A. J. (2016) Microstructural constraints on complex thermal histories of refractory CAI-like objects in an amoeboid olivine aggregate from the ALHA77307 CO3.0 chondrite. *Geochim. Cosmochim. Acta* **183**, 176–197.

Hashimoto A. and Grossman L. (1987) Alteration of Al-rich inclusions inside amoeboid olivine aggregates in the Allende meteorite. *Geochim. Cosmochim. Acta* **51**, 1685–1704.

Hua X., Adam J., Palme H. and El Goresy A. (1988) Fayalite-rich rims, veins, and halos around and in forsteritic olivines in CAIs and chondrules in carbonaceous chondrites: types, compositional profiles and constraints on their formation. *Geochim. Cosmochim. Acta* **52**, 1389–1408.

Ichimura S., Seto Y. and Tomeoka K. (2017) Nepheline formation in chondrite parent bodies: Verification through experiments. *Geochim. Cosmochim. Acta* **210**, 114–131.

Imae N. and Nakamuta Y. (2018) A new mineralogical approach for CO3 chondrite

characterization by X-ray diffraction: Identification of primordial phases and thermal history. *Meteorit. Planet. Sci.* **53**, 232–248.

Imai H. and Yurimoto H. (2003) Oxygen isotopic distribution in an amoeboid olivine aggregate from the Allende CV chondrite: Primary and secondary processes. *Geochim. Cosmochim. Acta* **67**, 765–772.

Itoh S., Kojima H. and Yurimoto H. (2004) Petrography and oxygen isotopic compositions in refractory inclusions from CO chondrites. *Geochim. Cosmochim. Acta* **68**, 183–194.

Jogo K., Nakamura T., Noguchi T. and Zolotov M. Yu (2009) Fayalite in the Vigarano CV3 carbonaceous chondrite: Occurrences, formation age and conditions. *Earth Planet. Sci. Lett.* **287,** 320–328.

Jones R. H. and Rubie D. C. (1991) Thermal histories of CO3 chondrites: Application of olivine diffusion modeling to parent body metamorphism. *Earth Planet. Sci. Lett.* **106,** 73-86.

Jurewicz A. J. G. and Watson E. B. (1988) Cations in olivine, Part 2: Diffusion in olivine xenocrysts, with applications to petrology and mineral physics. *Contrib. Mineral. Petrol.* **99**, 186–201.

Karato S. (1989) Grain growth kinetics in olivine aggregates. *Tectonophysics* **168**, 255–273.

Keller L. P. and Buseck P. R. (1990) Matrix mineralogy of the Lancé CO3 carbonaceous chondrite: A transmission electron microscope study. *Geochim. Cosmochim. Acta* **54**, 1155–1163.

Kimura M., Grossman J. N. and Weisberg M. K. (2008) Fe-Ni metal in primitive chondrites: Indicators of classification and metamorphic conditions for ordinary and CO chondrites. *Meteorit. Planet. Sci.* **43**, 1161–1177.

Komatsu M., Krot A. N., Petaev M. I., Ulyanov A. A., Keil K. and Miyamoto M. (2001) Mineralogy and petrography of amoeboid olivine aggregates from the reduced CV3 chondrites Efremovka, Leoville and Vigarano: Products of nebular condensation and accretion. *Meteorit. Planet. Sci.* **36**, 629–643.

Kojima T., Yada S. and Tomeoka K. (1995) Ca-Al-rich inclusions in three Antarctic CO3 chondrites, Yamato-81020, Yamato-820050 and Yamato-790992: Record of low-temperature alteration. *Proc NIPR Symp. Antarct. Meteor.* **8**, 79–96.

Krot A. N., Scott E. R. D. and Zolensky M. E. (1997) Origin of fayalitic olivine rims and lath-shaped matrix olivine in the CV3 chondrite Allende and its dark inclusions. *Meteorit.*

Planet. Sci. **32**, 31–49.

Krot A. N., Brearley A. J., Petaev M. I., Kallemeyn G. W., Sears D. W. G., Benoit P. H., Hutcheon I. D., Zolensky M. E. and Keil K. (2000) Evidence for low-temperature growth of fayalite and hedenbergite in MacAlpine Hills 88107, an ungrouped carbonaceous chondrite related to the CM-CO clan. *Meteorit. Planet. Sci.* **35**, 1365–1386.

Krot A. N., Petaev M. I. and Bland P. A. (2004) Multiple formation mechanisms of ferrous olivine in CV3 carbonaceous chondrites during fluid-assisted metamorphism. *Antarct. Meteor. Res.* **17**, 154–172.

Marinova M., Leroux H., Cuvillier P., Gloter A. and Jacob D. (2021) STEM-EELS investigation of planar defects in olivine in the Allende meteorite. *Minerals* **11**, 35.

McSween H. Y. Jr. (1977) Carbonaceous chondrites of the Ornans type: A metamorphic sequence. *Geochim. Cosmochim. Acta* **41**, 477–491.

Müller T., Dohmen R., Becker H., Ter Heege J. H. and Chakraborty S. (2013) Fe–Mg interdiffusion rates in clinopyroxene: experimental data and implications for Fe–Mg exchange geothermometers. *Contrib. Miner. Petrol.* **166**, 1563-1576.

Nomura K. and Miyamoto M. (1998) Hydrothermal experiments on alteration of Ca–Al-rich inclusions (CAIs) in carbonaceous chondrites: Implication for aqueous alteration in parent asteroids. *Geochim. Cosmochim. Acta* **62**, 3575–3588.

Palme H. and Fegley B. (1990) High-temperature condensation of iron-rich olivine in the solar nebula. *Earth Planet. Sci. Lett.* **101**, 180–195.

Rubin A. E. (1998) Correlated petrologic and geochemical characteristics of CO3 chondrites. *Meteorit. Planet. Sci.* **33**, 385–391.

Russell S. S., Huss G. R., Fahey A. J., Greenwood R. C., Hutchison R. and Wasserburg G. J. (1998) An isotopic and petrologic study of calcium-aluminum-rich inclusions from CO3 meteorites. *Geochim. Cosmochim. Acta* **62**, 689–714.

Schwinger S., Dohmen R. and Schertl H. (2016) A combined diffusion and thermal modeling approach to determine peak temperatures of thermal metamorphism experienced by meteorites. *Geochim. Cosmochim. Acta* **191**, 255–276.

Scott E. R. D. and Jones R. H. (1990) Disentangling nebular and asteroidal features of CO3 carbonaceous chondrite meteorites. *Geochim. Cosmochim. Acta* **54**, 2485–2502.

Sears D. W. G., Batchelor J. D., Lu J. and Keck B. D. (1991) Metamorphism of CO and CO-like

chondrites and comparisons with type 3 ordinary chondrites. *NIPR Symp. Antarct. Meteor.* **4**, 319–343.

Simon S. B., Krot A. N. and Nagshima K. (2019) Oxygen and Al-Mg isotopic compositions of grossite-bearing refractory inclusions from CO3 chondrites. *Meteorit. Planet. Sci.* **54**, 1362–1378.

Spandler C. and O'Neill H. St. C. (2010) Diffusion and partition coefficients of minor and trace elements in San Carlos olivine at 1,300°C with some geochemical implications. *Contrib. Mineral. Petrol.* **159**, 791–818.

Spandler C., O'Neill H. St. C. and Kamenetsky V. S. (2007) Survival times of anomalous melt inclusions from element diffusion in olivine and chromite. *Nature* **447**, 303–306.

Tomeoka K., Nomura K. and Takeda H. (1992) Na-bearing Ca-Al-rich inclusions in the Yamato-791717 CO carbonaceous chondrite. *Meteoritics* **27**, 136–143.

Wasson J. T., Yurimoto H. and Russell S. S. (2001) ^{16}O-rich melilite in CO3.0 chondrites: possible formation of common, 16O-poor melilite by aqueous alteration. *Geochim. Cosmochim. Acta* **65**, 4539–4549.

Weinbruch S., Palme H., Muller W. F. and El Goresy A. (1990) FeO-rich rims and veins in Allende forsterite: evidence for high temperature condensation at oxidizing conditions. *Meteoritics* **25**, 115–125.

Weisberg M. K. and Prinz M. (1998) Fayalitic olivine in CV3 chondrite matrix and dark inclusions: a nebular origin. *Meteorit. Planet. Sci.* **33**, 1087–1111.

Weisberg M. K., Zolensky M .E. and Prinz M. (1997) Fayalitic olivine in matrix of the Krymka LL3.1 chondrite: Vapor-solid growth in the solar nebula. *Meteorit. Planet. Sci.* **32**, 791–801.

Wick M. J. and Jones R. H. (2012) Formation conditions of plagioclase-bearing type I chondrules in CO chondrites: A study of natural samples and experimental analogs. *Geochim. Cosmochim. Acta* **98**, 140-159.

Zolotov M. Y., Mironenko M. V. and Shock E. L. (2006) Thermodynamic constraints on fayalite formation on parent bodies of chondrites. *Meteorit. Planet. Sci.* **41**, 1775–1796.

FIGURE CAPTIONS

Figure 1. BSE images of three Kainsaz AOAs (08, 34, and 75) that show well-developed Fe enrichments along olivine grain boundaries. Anorthite and diopside occur as common Ca,Al-rich phases enclosed in olivine aggregates. The dotted lines in (a-c) indicate the locations of FIB sections targeted for the TEM analysis. Abbreviations hereafter: ol = olivine, an = anorthite, di = diopside.

Figure 2. BSE images of one Kainsaz AOA (16) that shows heterogeneous Fe enrichments along olivine grain boundaries. The regions outlined in (a) are shown in detail in (b, c). Note a significant difference in Fe enrichments along olivine grain boundaries in these two sub-regions. There are FeO-rich olivine overgrowths at the AOA edge, as indicated by arrows in (b). The dotted lines in (b, c) indicate the locations of FIB sections targeted for the detailed TEM analysis.

Figure 3. BSE images of ferroan olivine overgrowths on olivine from Kainsaz AOAs. (a, b) Platy ferroan olivine overgrowths, indicated by arrows, on olivine in the AOA edges are present, with their elongation direction normal to the surfaces of the underlying olivine. (c) Platy ferroan olivine overgrowths occur around pore spaces in AOA olivines. Abbreviation hereafter: p = pores.

Figure 4. Fayalite contents (mol%) in olivine from eleven Kainsaz AOAs, in comparison with those from six ALHA77307 AOAs. All analyses were obtained using electron microprobe. Kainsaz AOA olivines have a broad range of $Fa_{\sim 1\text{-}22}$, but ALHA77307 AOA olivines show a very narrow range of $Fa_{<4}$.

Figure 5. Chromium concentrations in AOA olivines from Kainsaz and ALHA77307, obtained using electron microprobe. (a) A plot of Cr_2O_3 (wt%) vs. Fa (mol%). A dashed line indicates detection limits of electron microprobe analyses. (b) A histogram of Cr_2O_3 contents. Most Kainsaz AOA olivines contain $Cr_2O_3 \leq 0.1$ wt%, whereas most ALHA77307 AOA olivines contain 0.05-0.2 wt% Cr_2O_3.

Figure 6. Plot showing MnO (a) and Na_2O (b) contents (wt%) in AOA olivines from Kainsaz and ALHA77307, obtained using electron microprobe. The Na_2O and MnO contents have a slightly wider distribution in olivine from Kainsaz AOAs than from ALHA77307 AOAs. A weak correlation between MnO and Fa contents is present only in Kainsaz AOA olivines. Dashed lines indicate detection limits of electron microprobe analyses.

Figure 7. A DF-STEM mosaic of the FIB section from AOA 08 that shows dense olivine aggregates with highly equilibrated grain boundary textures. The Fe enrichment on olivine grain boundaries and the occurrence of chromite nanoparticles contribute to the bright contrast in this Z contrast image. Voids along olivine grain boundaries are indicated by arrows. Abbreviation hereafter: chr = chromite.

Figure 8. Distribution of Fe in olivine grains, obtained by TEM EDX. (a) BF-STEM image and corresponding Fe X-ray map of AOA 16. The FeO contents increase along olivine grain boundaries and cracks. The cracks are partially filled with chromite grains. (b) BF-STEM image and corresponding profile of fayalite (mol%) contents extracted from an olivine grain in AOA 16. The grain is strongly zoned, with more Fe enrichments towards the AOA edge.

Figure 9. A plot of MnO (wt%) vs. fayalite (mol%) contents of olivine from the host AOAs 16 and 75 and their overgrowth. Individual points represent single TEM EDX analyses. The olivine overgrowth contains higher MnO and fayalite contents, compared to the host olivine.

Figure 10. (a, b) BF-TEM images from AOAs 08 and 34 showing that abundant chromite nanoparticles (dark particles) decorate triple junctions between olivine grains. (c) BF-STEM image from AOA 16 showing needle-like chromite nanoparticles (dark particles) aligned along a single olivine grain boundary. (d) HRTEM image from AOA 08 of chromite nanoparticle in a crystallographic orientation relationship with the adjacent olivine. (e, f) FFT patterns extracted from (d) of the nanoparticle and adjacent olivine. The [110] zone axis of chromite is parallel to the [001] zone axis of olivine with $(111)_{chromite}//a_{olivine}$.

Figure 11. (a) BF-STEM image of chromite lamellae enclosed by ferroan olivine overgrowth at

the edge of AOA 16. All of the lamellae are elongated parallel to the c axis of olivine, as indexed from inset electron diffraction pattern of the ferroan olivine overgrowth. The chromite nanoparticles and a sulfide grain also occur at the overgrowth-host olivine interface. (b) False color TEM EDX map in Cr (yellow), Fe (red), Mg (green), and Si (blue) of a region outlined in (a). (c-e) HRTEM images of various chromite lamellae that share the same crystallographic orientation relationships with the surrounding olivine overgrowth. Inset FFT patterns in (c) are index as $(111)_{chromite}//a_{olivine}$, $[112]_{chromite}//b_{olivine}$, and $(110)_{chromite}//c_{olivine}$. Abbreviation: sf = sulfide.

Figure 12. (a, b) BF-STEM images and (c) false color TEM EDX map in Cr (red), Fe (blue), Mg (green), and Si (yellow) of thin chromite laths that grew into a pore space between olivine grains from AOA 16. A set of the chromite laths on the right of (a) are elongated parallel to the c axis of olivine, as indexed from inset electron diffraction patterns. In (b), note the presence of chromite nanoparticles, indicated by arrows, at the olivine edge. In (b, c), the chromite laths are surrounded by a thin layer of FeO-rich olivine. Abbreviation: Fe-ol: FeO-rich olivine.

Figure 13. (a) BF-STEM image of equant chromite inclusions in olivine grains from AOA 16. (b) HRTEM image from AOA 16 of the chromite grain with no crystallographic orientation relationship with the surrounding olivine. The upper inset is a lower-magnification BF-STEM image of the chromite grain used for HRTEM imaging, whereas the bottom inset is its FFT patterns, indexed as $[011]_{chromite}$.

Figure 14. Model zoning profiles for fayalite contents in olivine, based on the closed-system Fe^{2+}-Mg^{2+} interdiffusion between matrix, chondrule, and AOA minerals. We assumed that FeO contents in olivine and pyroxene from ALHA77307 represent initial compositions (Jones and Rubie, 1991). (a) The model profile for type I chondrule olivine, assuming that it is in direct contact with FeO-rich olivine in matrix during metamorphism. The profile shows much thicker diffusion depth and more FeO-rich composition at its rim, which is inconsistent with the observed olivine zoning profiles from type I chondrules in Kainsaz. (b) The model profile for type I chondrule olivine with the effect of the presence of a pyroxene rim, assuming that a total effective bulk diffusion coefficient of pyroxene is 1.5 times faster than a lattice diffusion

coefficient of olivine. This profile is a better fit for the observed olivine zoning profiles from type I chondrules in Kainsaz. (c) The model profile for type II chondrule olivine that experienced compositional exchange directly with FeO-rich olivine in matrix during metamorphism. (c) The model profile for matrix olivine. No effect of the presence of a pyroxene rim is expected on the model profiles for olivine in type II chondrule and matrix.

Figure 15. Model zoning profiles for Fe contents in olivine and diopside from Kainsaz AOAs. (a) The model profile for AOA olivine, assuming a simple global thermal metamorphism that is a feasible model for olivine zoning profiles measured from Kainsaz AOAs, as done for Fig. 14b. The calculations predict a flat profile for AOA olivine. (b) The model profile for AOA diopside, assuming a simple global thermal metamorphism, as done for Fig. 14b. Only a slight Fe enrichment at its edge is predicted. No effect of the presence of a pyroxene rim is expected on the model profiles for olivine and diopside in AOAs. (c) The model profile for AOA olivine, assuming a late-stage hydrothermal alteration after a global thermal metamorphism. We postulate a two-stage alteration scenario: (1) an initial complete equilibration of olivine ($Fa_{\sim 4\text{-}8}$) during peak thermal metamorphism at 500°C (solid line), followed by (2) a partial equilibration along the rim of an individual olivine grain driven by a late-stage diffusion during cooling from 500°C peak thermal metamorphism (dotted line). (d) The model profile for AOA olivine, based on cooling from variable peak temperatures of hydrothermal alteration after global thermal equilibration. We postulate a two-stage alteration scenario, as done for (c), but the second stage was calculated at lower peak temperatures of a late-stage hydrothermal alteration. The peak temperatures of 350°C, 300°C, and 200°C require 20 times, 1000 times, and 2×10^7 times faster Fe-Mg interdiffusion rates in olivine in a wet condition than in a dry condition.

Figure 16. Schematic scenario illustrating the possible alteration history of AOA olivines from Kainsaz. Temperature and time on the plot are not accurately scaled, only as a reference to show a sequence of a series of alteration events. A timing for the accretion of CO3 chondrite parent body and the formation of ferroan olivine overgrowths was estimated based on Doyle et al. (2015). We propose the following sequence: (1) the mobilization of Si, Al, Cr, Fe, and Mg with the onset of thermal metamorphism; (2) the initial equilibration of AOA olivines at $Fa_{\sim 4\text{-}8}$ during peak thermal metamorphism; (3) the formation of steep Fe enrichments up to $Fa_{\sim 31}$ along the

edges of AOA olivines on cooling after peak thermal metamorphism; (4) the exsolution and epitaxial growth of chromite; and (5) the ferroan olivine overgrowths onto the AOAs.

Figure 1

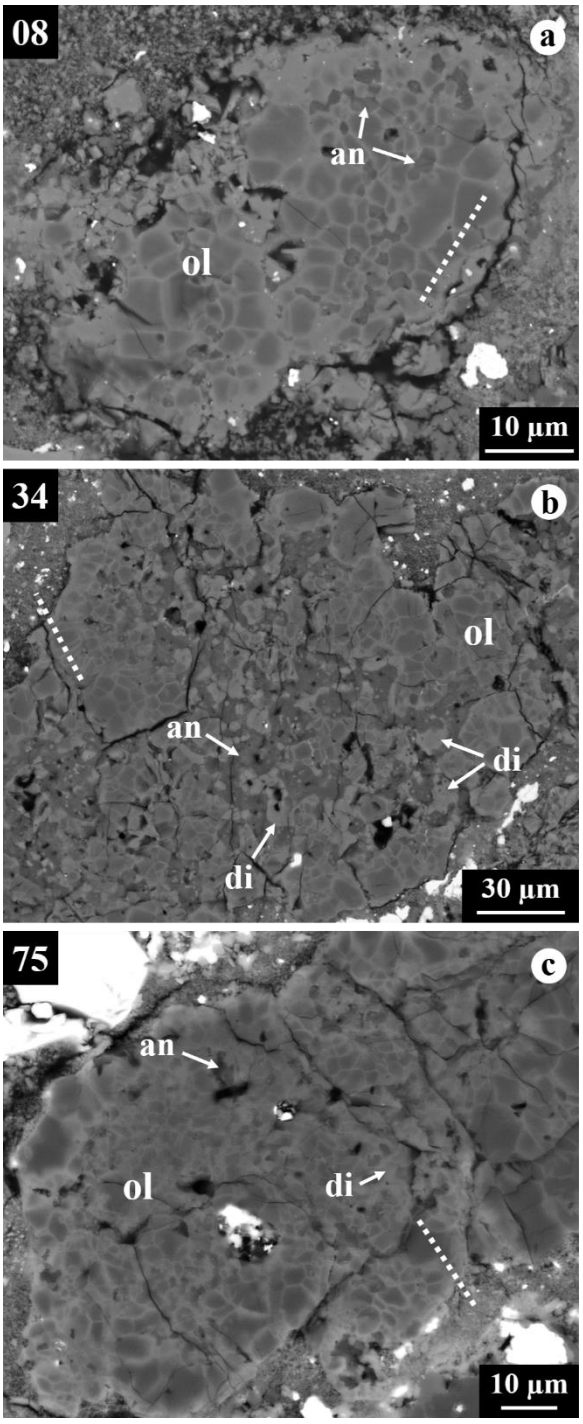

1073 Figure 2

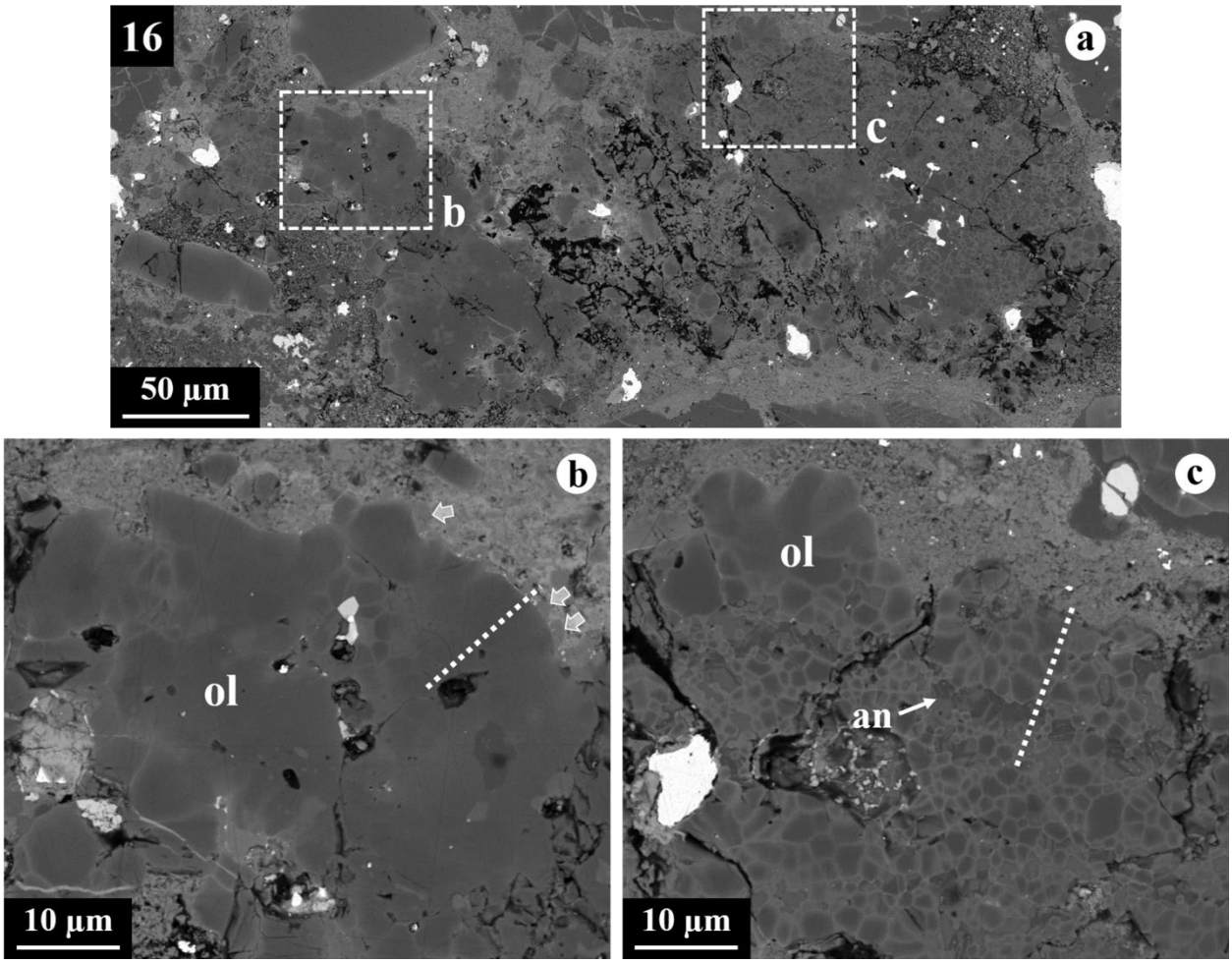

1074

1075 Figure 3

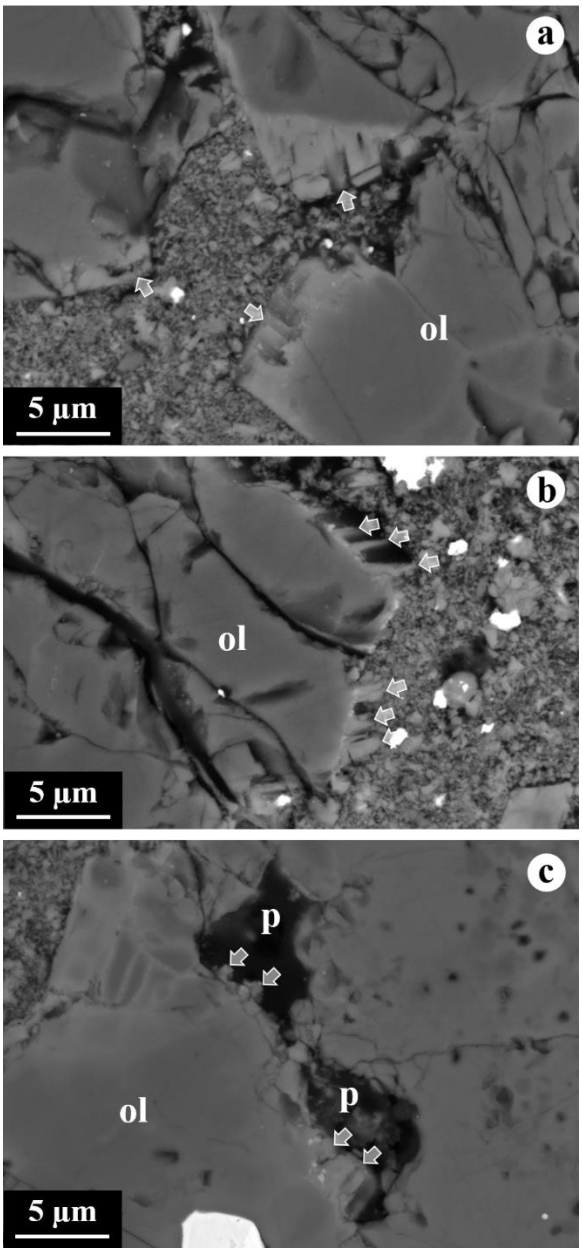

1076

1077 Figure 4

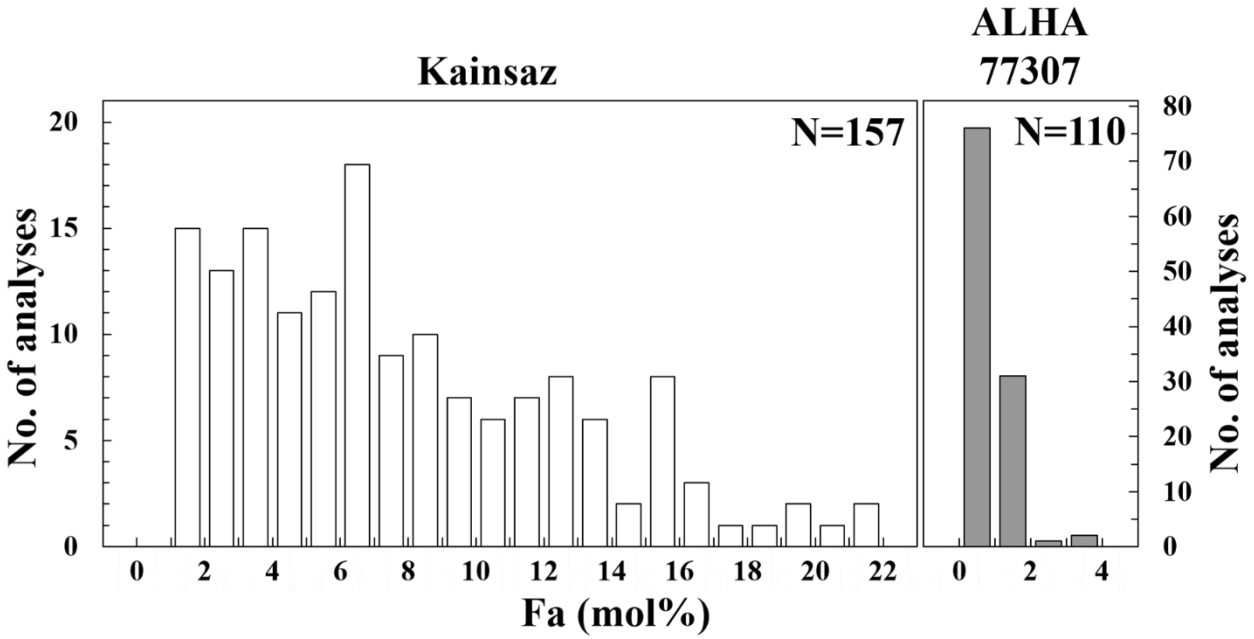

1078

1079 Figure 5

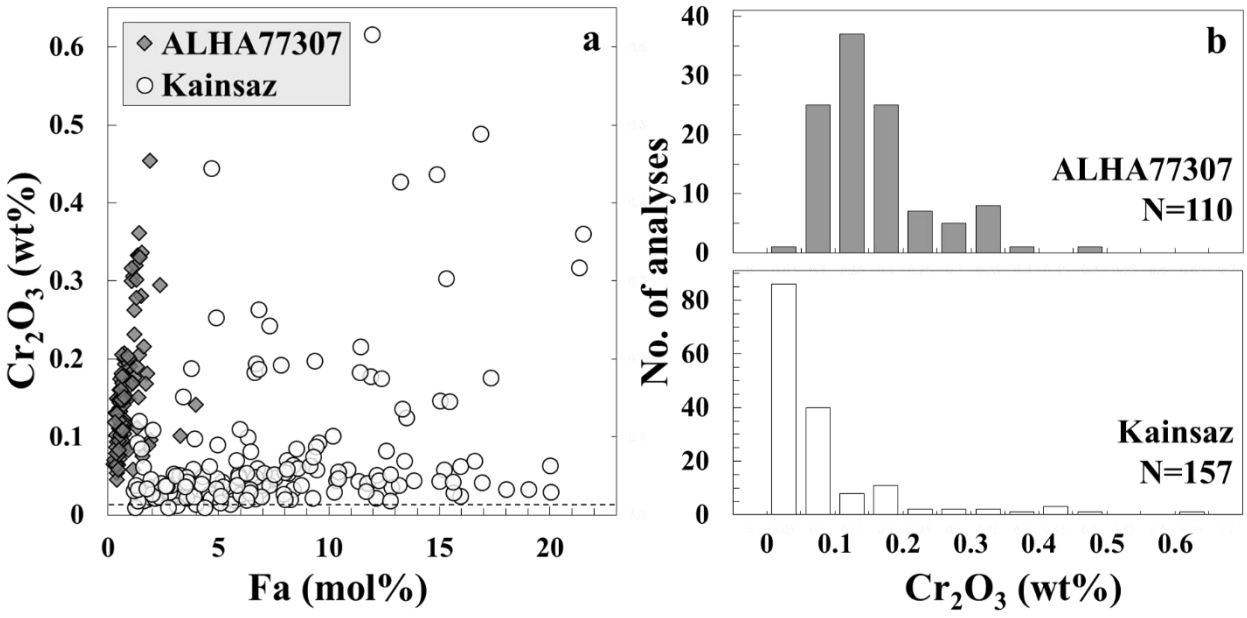

1080

1081 Figure 6

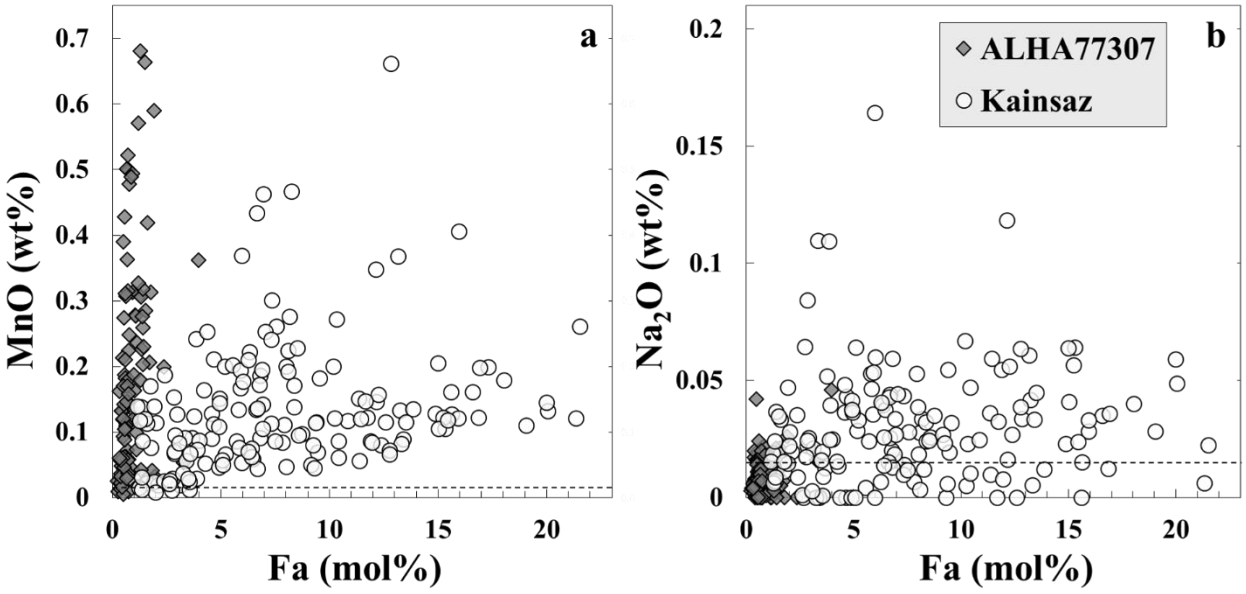

1082

1083

1084 Figure 7

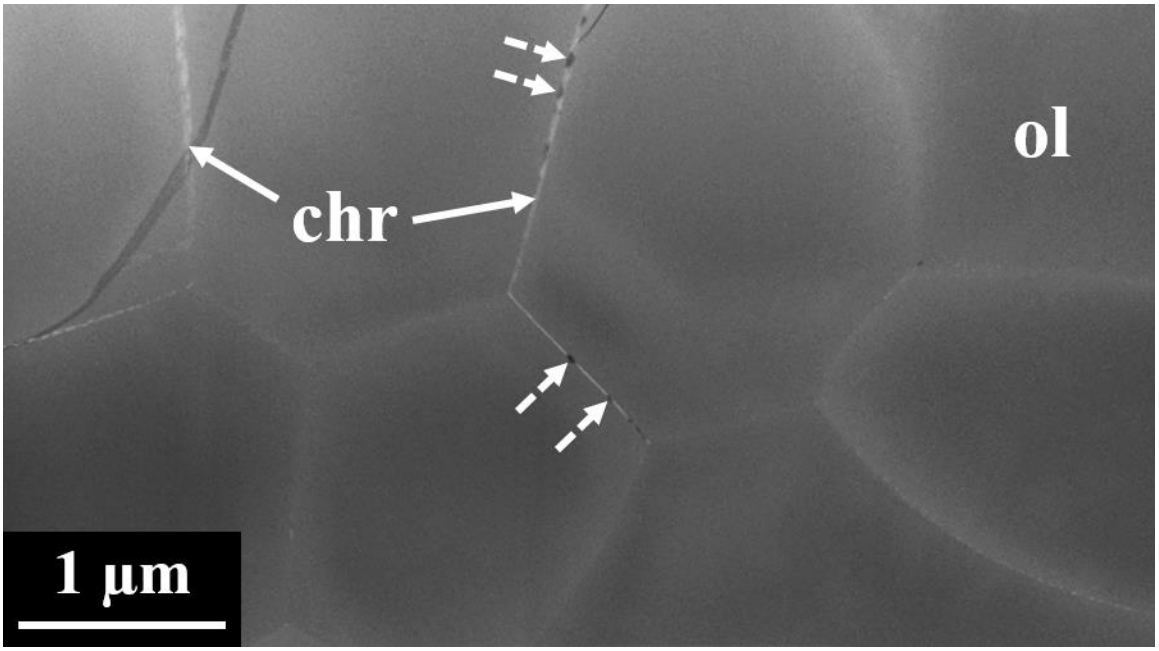

1085

1086 Figure 8

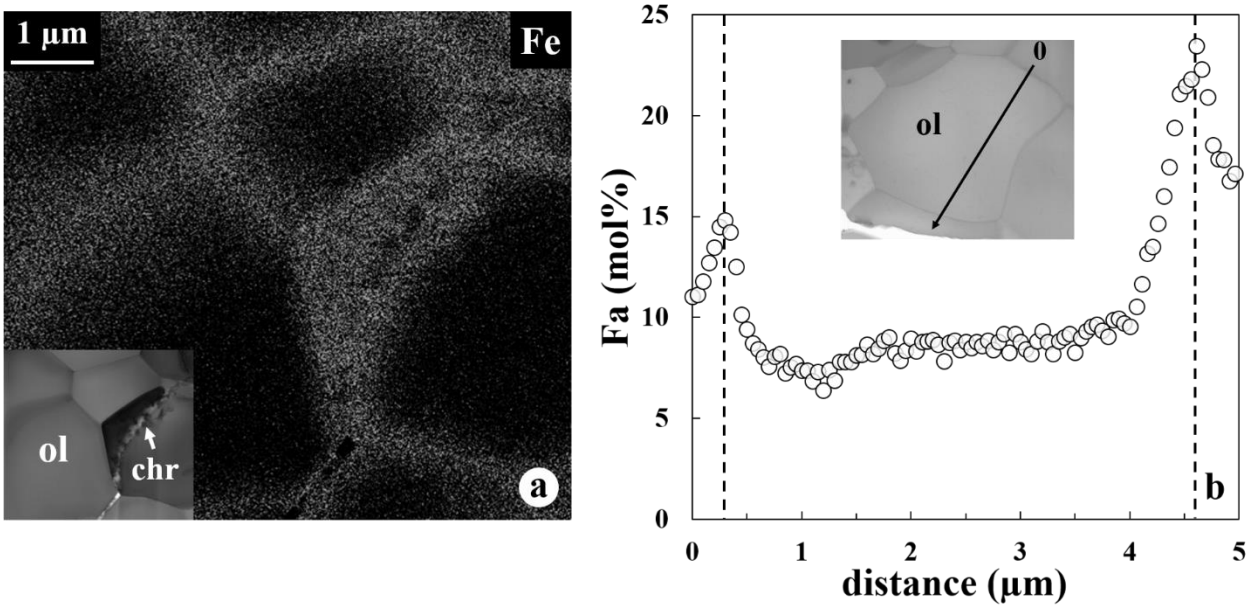

1087

1088

1089 Figure 9

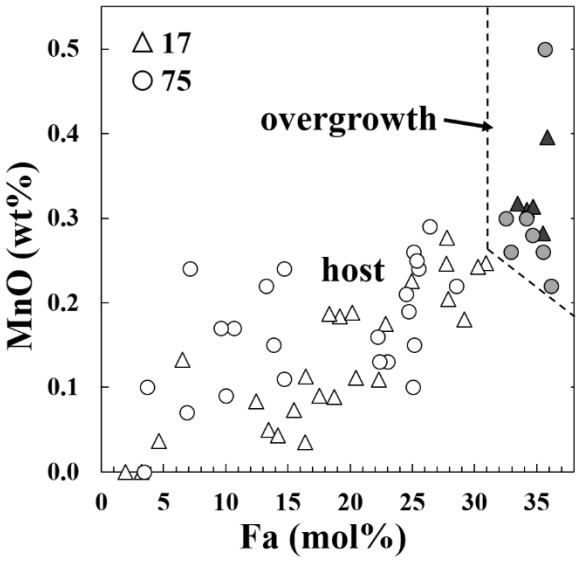

1090

1091 Figure 10

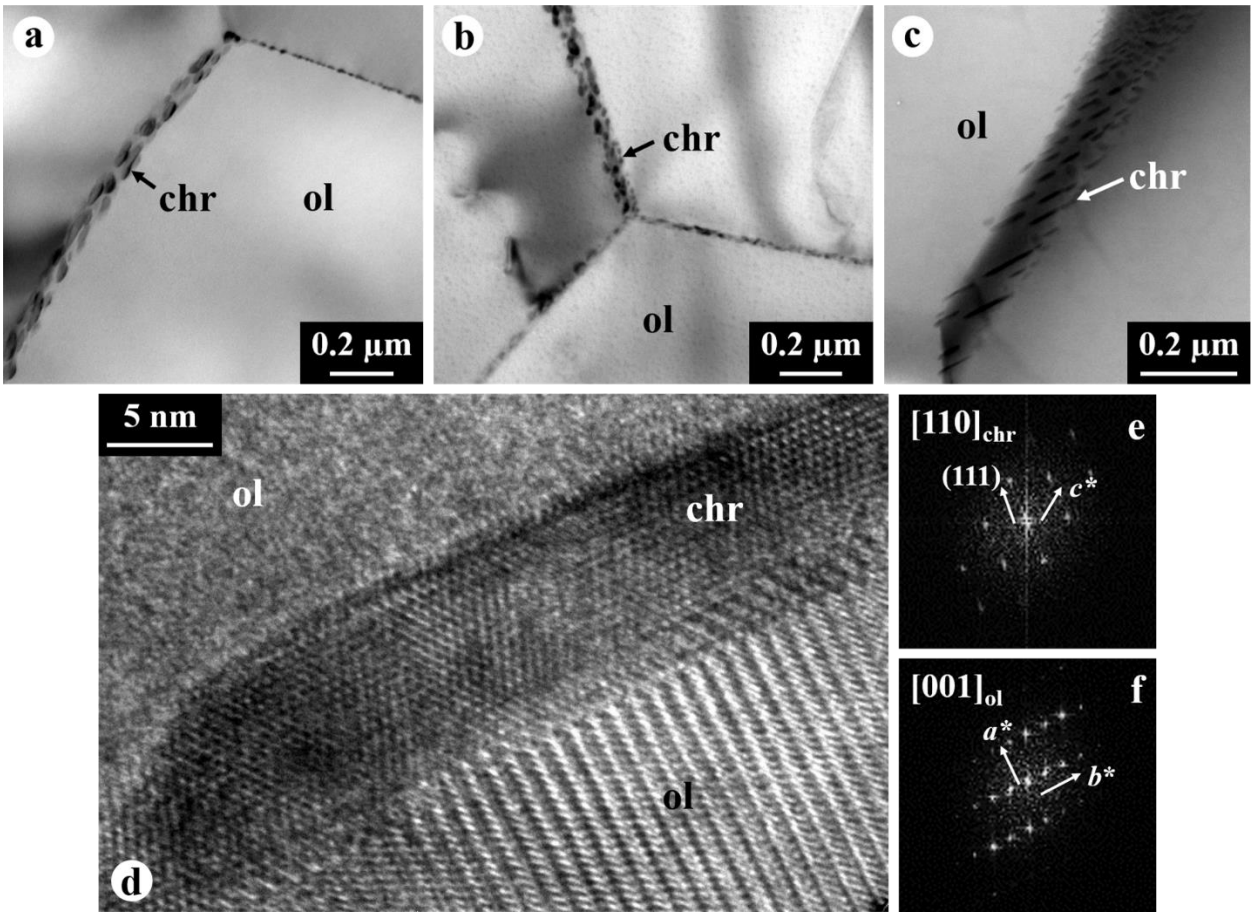

1092

Figure 11

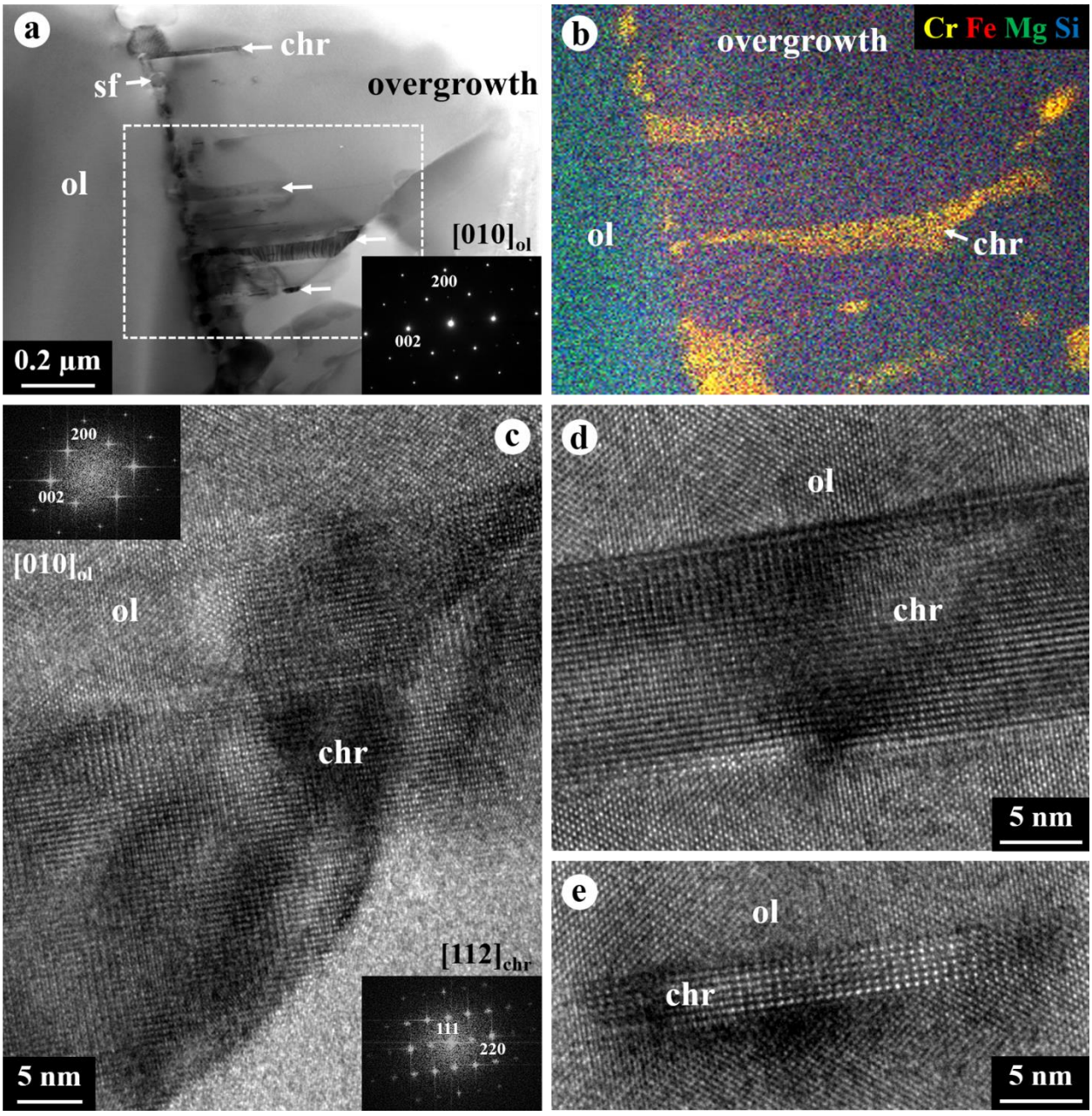
a
chr
sf
overgrowth
ol
[010]ol
200
002
0.2 µm
b
overgrowth
Cr Fe Mg Si
ol
chr
200
002
c
[010]ol
ol
chr
[112]chr
111
220
5 nm
d
ol
chr
5 nm
e
ol
chr
5 nm

Figure 12

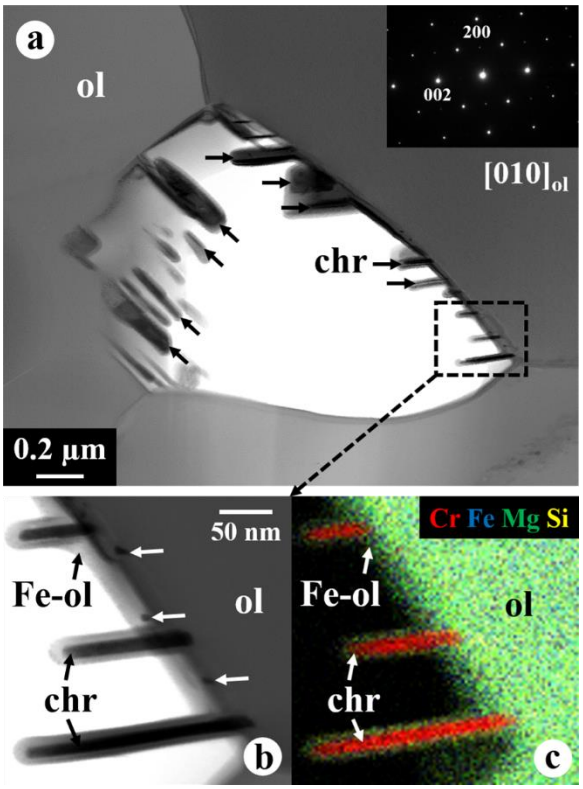
a
ol
200
002
[010]ol
chr
0.2 µm
50 nm
Fe-ol
ol
chr
b
Cr Fe Mg Si
Fe-ol
ol
chr
c

1097 Figure 13

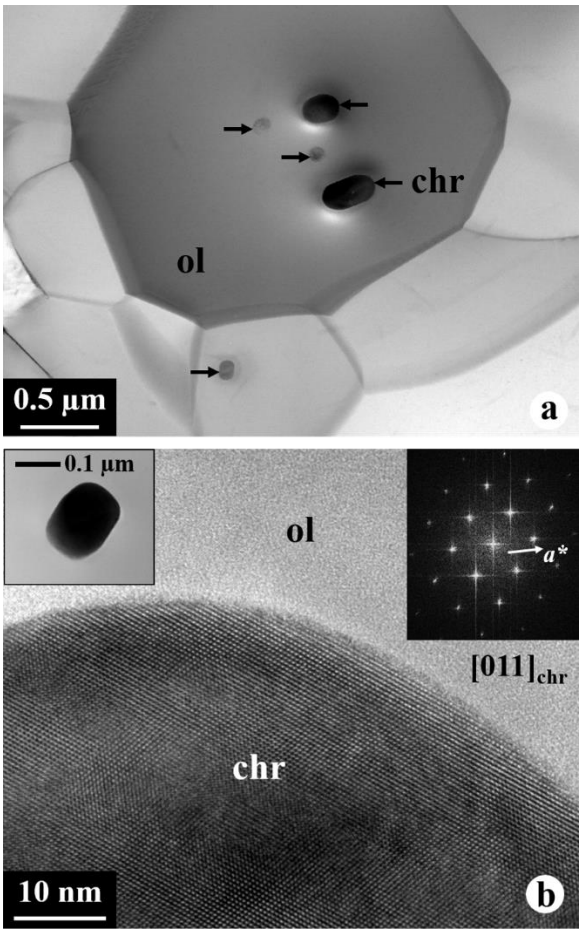

1098

Figure 14

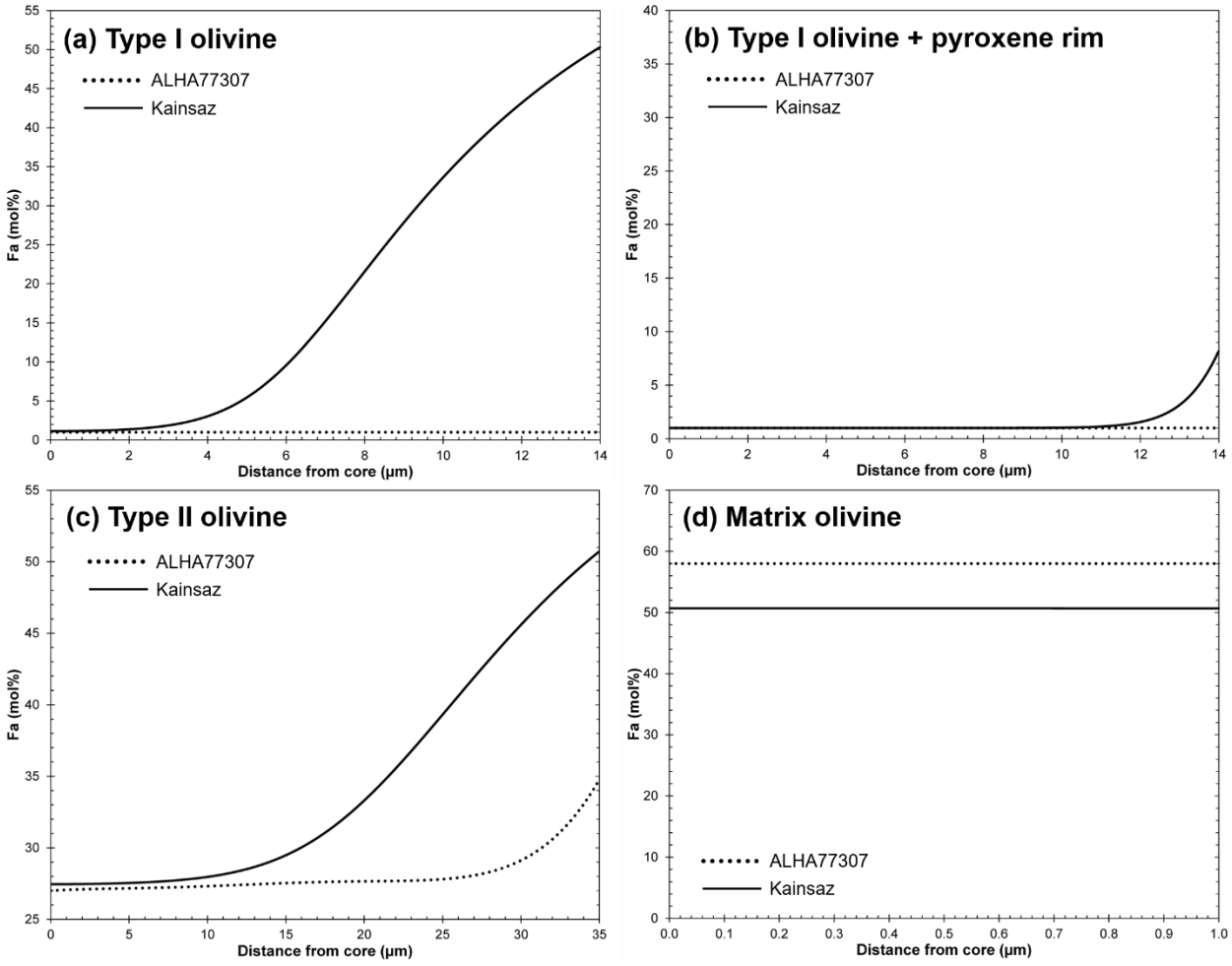
(a) Type I olivine
ALHA77307
Kainsaz
Fa (mol%)
Distance from core (μm)
(b) Type I olivine + pyroxene rim
ALHA77307
Kainsaz
Fa (mol%)
Distance from core (μm)
(c) Type II olivine
ALHA77307
Kainsaz
Fa (mol%)
Distance from core (μm)
(d) Matrix olivine
ALHA77307
Kainsaz
Fa (mol%)
Distance from core (μm)

Figure 15

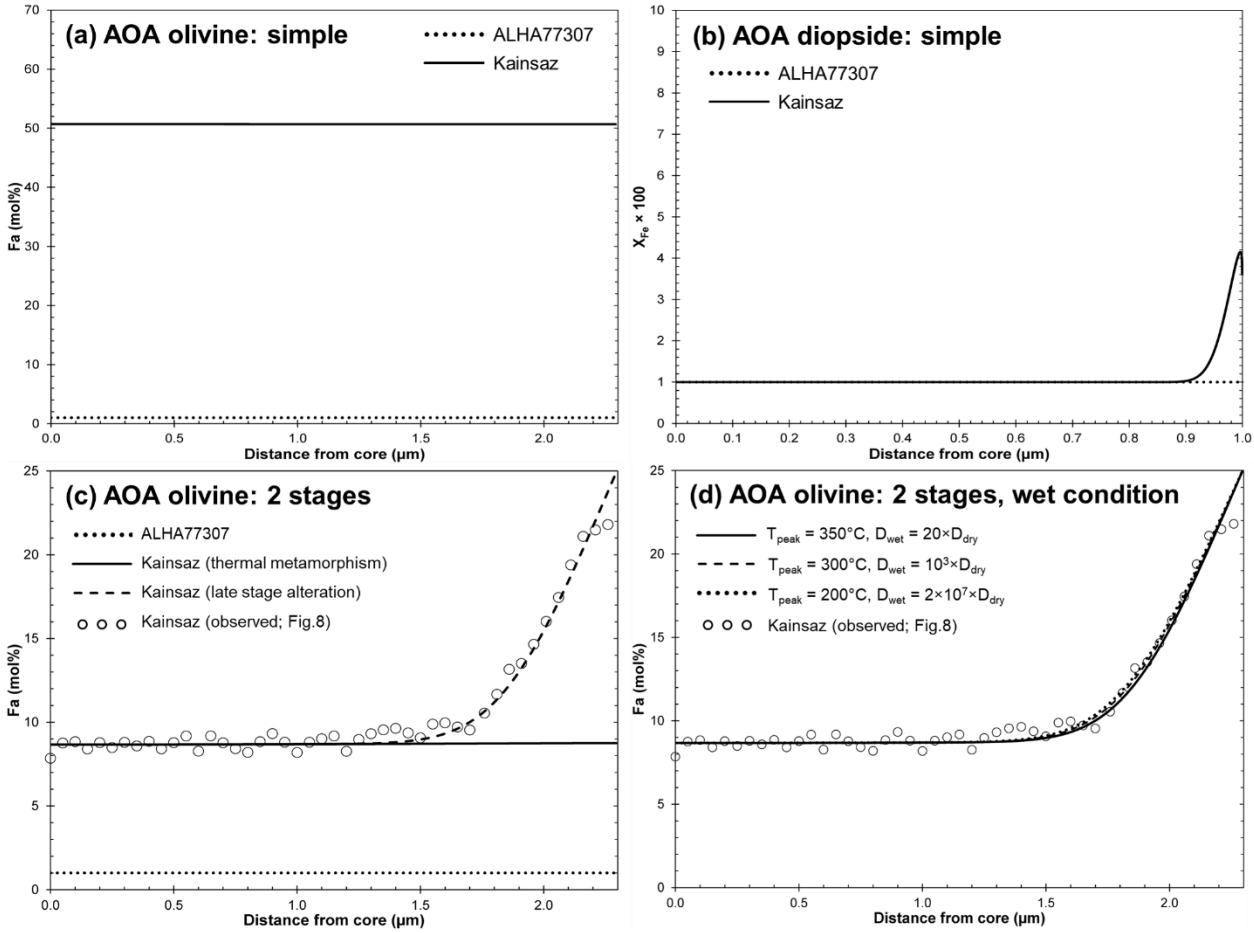
(a) AOA olivine: simple
ALHA77307
Kainsaz
Fa (mol%)
Distance from core (μm)
(b) AOA diopside: simple
ALHA77307
Kainsaz
X_{Fe} × 100
Distance from core (μm)
(c) AOA olivine: 2 stages
ALHA77307
Kainsaz (thermal metamorphism)
Kainsaz (late stage alteration)
Kainsaz (observed; Fig.8)
Fa (mol%)
Distance from core (μm)
(d) AOA olivine: 2 stages, wet condition
T_{peak} = 350°C, D_{wet} = 20×D_{dry}
T_{peak} = 300°C, D_{wet} = 10^3×D_{dry}
T_{peak} = 200°C, D_{wet} = $2×10^7$×D_{dry}
Kainsaz (observed; Fig.8)
Fa (mol%)
Distance from core (μm)

1103 Figure 16

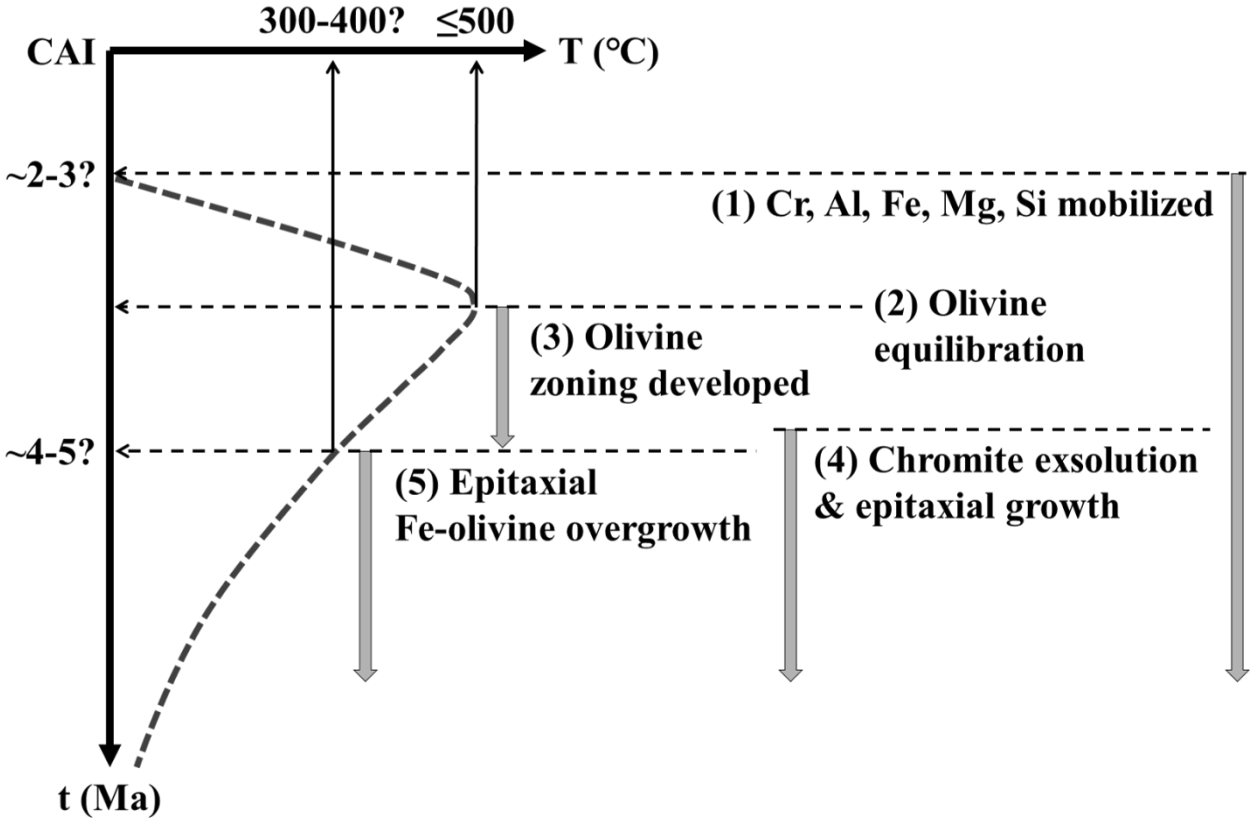

1104